

## Fatigue crack propagation in functionally graded bi-material steel obtained through wire-arc additive manufacturing

Galán Argumedo, J. L.; Suresh, A.; Ding, Z.; Bertolo, V.; Reinton, T. E.; Riems slag, A. C.; Hermans, M. J.M.; Popovich, V. A.

**DOI**

[10.1016/j.ijfatigue.2025.108819](https://doi.org/10.1016/j.ijfatigue.2025.108819)

**Publication date**

2025

**Document Version**

Final published version

**Published in**

International Journal of Fatigue

**Citation (APA)**

Galán Argumedo, J. L., Suresh, A., Ding, Z., Bertolo, V., Reinton, T. E., Riems slag, A. C., Hermans, M. J. M., & Popovich, V. A. (2025). Fatigue crack propagation in functionally graded bi-material steel obtained through wire-arc additive manufacturing. *International Journal of Fatigue*, 194, Article 108819. <https://doi.org/10.1016/j.ijfatigue.2025.108819>

**Important note**

To cite this publication, please use the final published version (if applicable).  
Please check the document version above.

**Copyright**

Other than for strictly personal use, it is not permitted to download, forward or distribute the text or part of it, without the consent of the author(s) and/or copyright holder(s), unless the work is under an open content license such as Creative Commons.

**Takedown policy**

Please contact us and provide details if you believe this document breaches copyrights.  
We will remove access to the work immediately and investigate your claim.



# Fatigue crack propagation in functionally graded bi-material steel obtained through wire-arc additive manufacturing

J.L. Galán Argumedo<sup>\*</sup>, A. Suresh<sup>✉</sup>, Z. Ding, V. Bertolo, T.E. Reinton, A.C. Riemsdag, M.J.M. Hermans, V.A. Popovich

Department of Materials Science and Engineering, Delft University of Technology, the Netherlands

## ARTICLE INFO

### Keywords:

Wire arc additive manufacturing  
Bi-metallic additively manufactured structures  
Fatigue crack propagation

## ABSTRACT

This study concentrates on the fatigue crack propagation behaviour of a high-strength low-alloy (HSLA) steel and austenitic stainless (AS) steel bi-material part, as obtained by wire arc additive manufacturing (WAAM). Due to partial mixing in the weld pool, the first layer of AS steel laid onto the previously deposited HSLA steel results in a diluted interface layer of distinct chemical and microstructural characteristics. Average Paris parameters are obtained for the interface layer along transverse and longitudinal planes to the deposition direction (BD-LD plane:  $m = 2.79$ ,  $\log_{10}(C) = -7.83 \log_{10}(da/dN)$ ) (BD-TD plane:  $m = 3.47$ ,  $\log_{10}(C) = -8.39 \log_{10}(da/dN)$ ). However, it is observed that this interface layer manifests an intriguing crack propagation behaviour. FCGR consistently drop as the crack front transitions from undiluted AS steel to the interface. At  $\Delta K = 20 \text{ MPa}\cdot\text{m}^{0.5}$ , the greatest  $\Delta$  is  $-0.77 \log_{10}$  steps ( $R = 0.1$ ). As cracks near the HSLA fusion line, rates re-accelerate up to  $+0.75 \log_{10}$  steps ( $R = 0.5$ ). The phenomenon is attributed to the interplay between deformation-induced martensitic transformation and pre-existing allotropic martensite. Our findings, derived from a series of fatigue tests in correlation with multiscale microstructural and fracture characterization, offer insights into the damage-tolerant behaviour of these bi-material structures.

## 1. Introduction

Functional grading of metal parts through additive manufacturing (AM) proves to be an effective approach to overcome conventional limitations in material performance. Examples range across several functional properties, although notable work shows e.g., a balance between strength and ductility [1], grain size and fretting resistance [2], creep and thermomechanical fatigue [3], tuned fatigue crack propagation resistance [4], as well as excellent mechanical and oxidation properties at high temperatures [5]. Many more examples are provided in relevant reviews, such as the one from Zhang *et al.* [6]. Between the different AM methods, wire arc additive manufacturing (WAAM) offers an approach to manufacture functionally graded components of large dimensions, demonstrably up to the meter-scale [7]. Profiting from the flexibilities in process parameters, large deposition rates, and a vast array of available wire compositions, it is possible to manufacture highly optimized large-scale parts that can adequately perform in ever more demanding environments.

An approach to achieve functional grading is to additively

manufacture compositionally graded structures. With this approach, the desired functional properties are obtained by grading the chemical composition across a part's volume [8]. Along many possible combinations, the pairing of high-strength low-alloy (HSLA) steel and austenitic stainless (AS) steel is deemed interesting. Numerous studies have shown the potential that WAAM offers to manufacture fully dense HSLA steel structures with excellent mechanical properties [9,10]. However, HSLA steels face severe disadvantages. These include susceptibility to corrosion, as well as ductile to brittle transition at low temperatures. A technique to overcome this problem is to functionally-grade HSLA steel structures with a corrosion-resistant material [11], such as an AS steel [12]. Thanks to the addition of Cr and Ni, the latter family of steel alloys displays a stable austenite phase with excellent corrosion and mechanical performance at a wide range of temperatures.

Compositional gradients through WAAM can be achieved by several approaches. These can take the form of stepped gradients [13,14], sharp interfaces by direct joining of two dissimilar alloys [15], or dissimilar joining by means of an intermediate layer of a third alloy [16,17]. The selection of the most appropriate strategy is typically based on the

<sup>\*</sup> Corresponding author.

E-mail address: [j.l.galanargumedo@tudelft.nl](mailto:j.l.galanargumedo@tudelft.nl) (J.L. Galán Argumedo).

tolerance of the selected alloys to mix with each other, and the microstructural constituents derived therefrom. Previous attempts have demonstrated that it is possible to pair HSLA and AS steel alloy families into a bi-material additively manufactured structure (BAMS) [18,19]. This was achieved without the need of an intermediate layer or a stepped gradient.

Making a bi-material part of HSLA steel and AS steel through WAAM does impose certain challenges. Considerable dilution takes place as the first layer of a highly alloyed stainless steel is deposited onto a low-alloyed steel substrate. Partial mixing in the weld pool leads to inhomogeneities in chemical composition. Consequently, heterogeneities are expected in the microstructural make-up of the diluted layer [20]. The nature of these heterogeneities depends on the local chemical make-up. The dilution of Ni may lead to a higher fraction of ferrite-promoting components, such as Cr and Si. This entails a higher ferrite fraction across the bulk of the interface weld metal [21]. Highly localized dilution may even lead to the formation of martensite at room temperature. This has been reported frequently as a band running along the fusion line or in the form of islands [22,23]. Also, a chemical potential is formed between the adjacent AS and the HSLA ferritic layers, leading to carbon migration after prolonged thermal treatment [12,24]. This process can lead to an excessively hard carburized austenite and a soft ferrite phase with low creep resistance. For the reasons mentioned, this diluted layer (hereon simply referred to as the interface) is of special interest.

Limited work has been done to characterize the mechanical behaviour of HSLA-AS steel BAMS. Tensile tests of bi-metal tensile coupons shown by Ahsan *et al.* in two related studies [21,25] show that necking and failure are typically localized away from the interface layer. This is confirmed in similar studies by Ayan *et al.* [26], and Suárez *et al.* [27]. Repetition of quasi-static mechanical testing with the aid of digital image correlation shows a change in the work-hardening behaviour at the interface. Instead of a monotonic decay in work-hardening rate, the interface develops a local minimum and subsequent strengthening originating from strain-induced martensitic transformation. This is otherwise known as TRIP effect and is attributed to the local chemical constitution of the interface material [28]. In terms of fatigue, Ayan *et al.* [26] showed that HSLA-AS steel bi-material parts display adequate behaviour under bending stresses, as failure typically originated on the HSLA material volume. Nonetheless, no further research is apparently available on the fatigue crack propagation behaviour. This is necessary, as the mechanisms controlling deformation ahead of a crack tip across the interface layer are observed to be different from the parent materials.

It is crucial to understand the fatigue crack propagation behaviour for a reliable application of HSLA-AS steel BAMS. The intention of this study is to establish empirical evidence on the fatigue behaviour of bi-metal components specific to the metallurgical conditions obtained from the WAAM process. Benchmarking results are carried out for mono-material specimens of ER70S-6 (HSLA steel) and ER316L (AS steel) and are used to establish a performance baseline. Fatigue crack propagation studies are then carried out across interface layer to understand its behaviour in the context of a bi-metal part. Microscopy, fractography and electron backscatter diffraction are used to understand the relationship between microstructure and fatigue performance. Special attention is placed on the martensite found along the interface as an outcome of the AM process, and its effect as a crack-accelerating microstructural feature. These results are fundamental to establish workable reliability levels, and to adequately estimate their fatigue life performance.

## 2. Materials and method

### 2.1. Wire arc additive manufacturing

Wire arc additive manufacturing of a bi-material block was carried out with a 6-degree of freedom robot and a CMT-capable Fronius power

source. The chemical specification of the wire consumables is provided in Table 2-1. With these consumables, a block of width 127 mm, height 91 mm and length 205 mm was additively manufactured. Deposition parameters are included in Table 2-2. The first 54 mm of height (16 layers) were deposited with HSLA steel and the remaining 37 mm (16 layers) were deposited with AS steel. Before changing the wire consumable, the top of the block was machined to ensure a flat interface layer. All beads in a single layer were deposited in the same orientation. This orientation was alternated per layer to avoid bulk-ups at the start-stop locations. This is schematically shown in Fig. 2-1 (a). Mechanical properties of both undiluted materials are included in Table 2-3 after being deposited. Mechanical properties of the bi-material interface are also included, although the reader is referred to Galán Argumedo *et al.* [29] for further details on how these results were obtained. This source provides a detailed microstructural characterization relevant to the interface layer.

### 2.2. Fatigue specimens, testing apparatus and programme

Single edge notched bending (SENB) specimens were extracted from the bi-material block for fatigue testing. Prisms with dimensions of length 60 mm, width  $W$  of 10 mm, and thickness  $B$  of 5 mm were obtained by cutting and milling. Dimensions are intentionally chosen small to minimize the effect of residual stresses on the fatigue crack growth rate (FCGR) measurements [32]. The prisms were obtained in two orientations designated transverse and longitudinal to capture the anisotropic effect caused by the deposition strategy. Mono-material specimens were extracted from the HSLA and AS steel material volumes. This was done at a minimum distance of 10 mm away from the dissimilar fusion line to avoid any effect of dilution. Bi-material specimens were extracted in such way that a portion of the interface would be contained within their volume, and such that the dissimilar fusion line would be located at a maximum distance of 6 mm from the face intended for notching. A starter notch of 1.5 mm length and 0.4 mm width was fabricated through electric discharge machining. The top face was notched on all specimens, intending a consistent crack propagation direction opposite to the building direction (BD). The specimen dimensions, orientations and distribution within the bi-material parent block are pictured on Fig. 2-1 (b).

A fatigue-rated testing apparatus was used to carry out the fatigue testing program. Force-controlled cyclic loading was applied using a servo-hydraulic MTS frame with a load range of  $\pm 25$  kN. The frame was controlled with an MTS MultiPurpose TestWare and Flextest electronic control unit. Direct current potential drop (DCPD) measurements were done with dedicated DCPD Howden hardware at a crack length extension resolution of 50  $\mu\text{m}$ . A polymer clamp system was used to facilitate stable and consistent connection points of the DCPD probes. The specimen, polymer clamp, electrical probes and loading frame are pictured on Fig. 2-1 (c). DCPD set-up calibration was done per material (HSLA steel/AS steel/bi-material). In the case of the bi-material specimens, calibration was also carried out based on specimen orientation. Calibration involved the polynomial regression of the data pairs voltage vs. crack extension, as measured every 0.5 mm. Crack increments were observed with a long-distance stereo microscope and physical markings on a polished face of the specimen. DCPD measurements were done in

**Table 2-1**

Chemical composition of wire materials as stated by manufacturer, in wt% [30,31].

	C	Si	Mn	Cr	Ni	Mo	N	Fe
3Dprint AM 46 (ER70S-6 HSLA steel)	0.1	1.00	1.7	–	–	–	–	Bal.
3Dprint AM 316L (ER316L AS steel)	0.015	0.45	1.6	18.5	12.0	2.6	0.04	Bal.

**Table 2.2**

Target voltage (U) and current (I), Wire Feed Speed (WFS), Travel Speed (TS) Contact Tip Working Distance (CTWD) Heat Input (HI), and Interpass Temperature (Int. Temp.) deposition parameters for the different wire consumables used.

	target U	target I	WFS	TS	CTWD	HI	Int. Temp.
	V	A	m/min	mm/s	mm	kJ/mm	°C
3Dprint AM 46 (HSLA)	21.1	143	7.5	10	17	0.27	50–120
3Dprint AM 316L (ASS)	13.2	214	5.0	10	17	0.22	<140

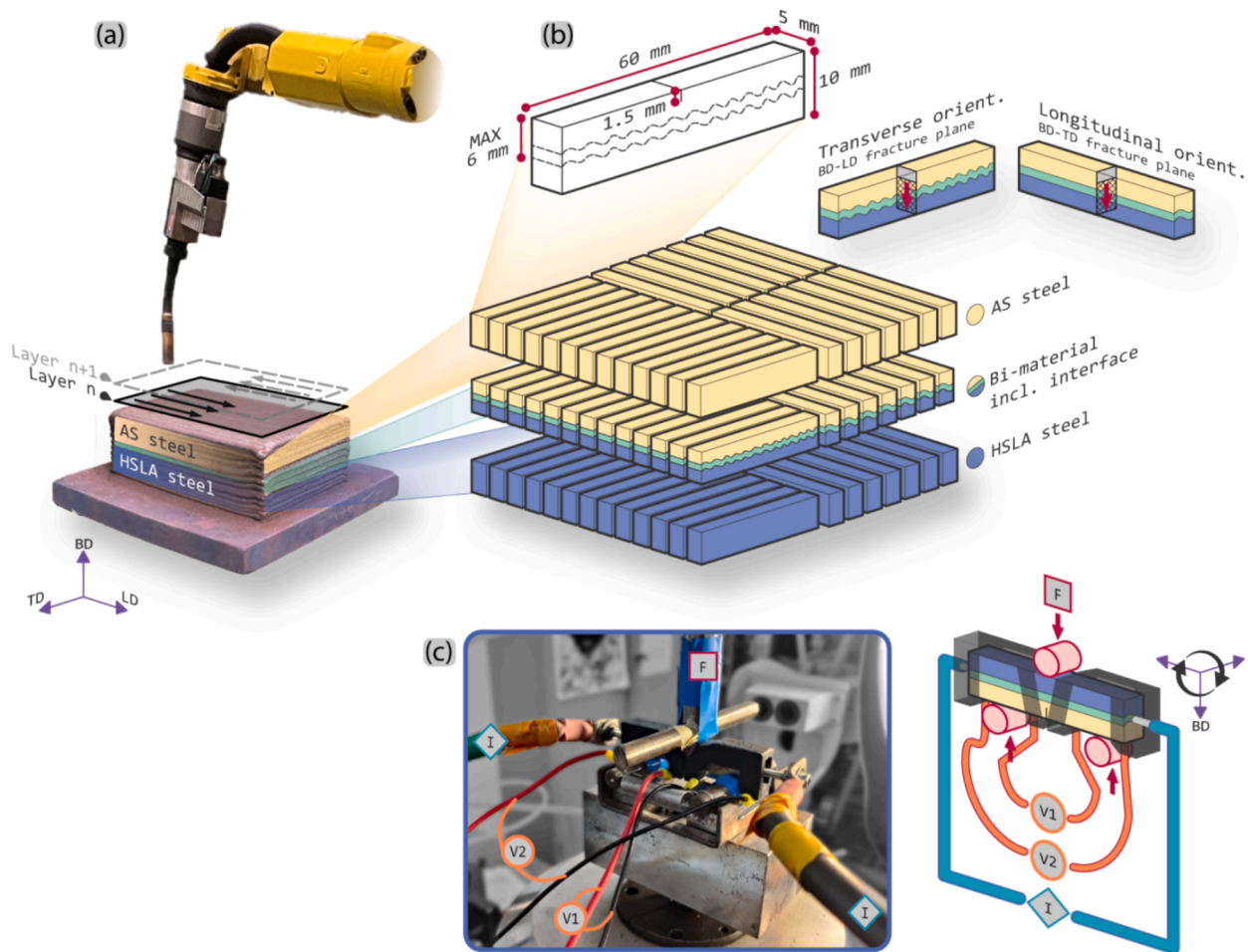


**Fig. 2–1.** (a) WAAM layer deposition strategy of bi-material block. (b) Sample distribution within parent block, as well as dimensions, materials, and orientations used for testing. (c) Testing set-up used for FCGR measurement for single edge notched 3-point bending specimens with DCPD measurement probes connected. Note the specimen is placed upside-down during testing. Diagram indicates potential drop measurement location about the crack tip (V1) and reference circuit (V2), alongside location of current-carrying leads (I). Contact rollers belonging to the load train (F) are also shown for context. Sketches are not to scale.

**Table 2.3**

Mechanical properties of wire consumables as obtained from as-deposited WAAM’ed tensile coupons [29].

	Elastic Modulus E [GPa]	Yield Strength $s_y$ [MPa]	Tensile Strength $s_u$ [MPa]	Elongation at fracture $\Delta/L_0$ [%]
3Dprint AM 46 (ER70S-6 HSLA steel)	197 ± 6	608 ± 7	683 ± 9	24.5 ± 2.1
Diluted interface	157 ± 17	412 ± 13	592 ± 11	19.8 ± 4.9 (*)
3Dprint AM 316L (ER316L AS steel)	154 ± 8	418 ± 5	548 ± 4	29.7 ± 1.3

(\*) Necking occurs outside of gauge length.

agreement with ISO 12108 [33]. While testing, data was recorded continuously at a frequency of 100 Hz. An averaging data algorithm was used to reduce data to every 0.01 mm of crack extension, either based on time–voltage acquisition or peak-valley computations, as deemed more appropriate depending on the nature of fatigue test being performed.

A sharp fatigue crack tip was obtained by means of pre-fatigue. Specimen pre-fatiguing was done following a reducing  $\Delta K$  procedure. To do so, a decreasing  $\Delta K$  relationship was employed following:

$$\Delta K = \Delta K_0 \exp[C(a - a_0)] \quad (1)$$

where  $\Delta K$  is the applied stress intensity range,  $\Delta K_0$  is the initial  $\Delta K$  value set at 25 MPa·m<sup>0.5</sup>,  $C$  is the reduction gradient set at an approximate value of  $-0.02 \text{ mm}^{-1}$ ,  $a_0$  is the starting notch length and  $a$  is the instantaneous crack length. For single-material specimens,  $\Delta K = K_{MAX} - K_{MIN} = K(P_{MAX}) - K(P_{MIN})$  was determined based on standard relationships such that,

$$K = \left[ \frac{P \cdot S}{B \cdot W^{3/2}} \right] \cdot f\left(\frac{a}{W}\right) \quad (2)$$

where  $P$  is either the  $K_{MAX}$  or  $K_{MIN}$  applied load, and  $S$  is the span between supports equal to  $4 \cdot W$ . The function  $f(a/W)$  is the geometry-dependent relation between the load applied and the stress intensity value, as provided on ISO 12108 [33]. For mono-material specimens, these relationships are sufficient to determine every value of  $K$ . For bi-material specimens, a modification of the standard relationship is necessary, such that:

$$K_{BM} = \sqrt{\Gamma_f^E} \cdot K \quad (3)$$

given that  $\Gamma_f^E$  is a correction function derived from the numerical FEM analysis of bi-material SENB specimens.  $\Gamma_f^E$  is a function of elastic moduli  $E$  of the materials involved, crack length  $a$ , and position of the bi-material dissimilar fusion line  $Z(BM)$ . The derivation and function values of  $\Gamma_f^E$  are provided in Annex A1. In every case,  $K_{MAX}$  at the end of the pre-fatigue procedure was lower than the  $K_{MAX}$  at the start of the fatigue test, as dictated by standard procedure [33].

Three testing programmes were carried out to characterize the fatigue crack propagation behaviour of the bi-material block. These programmes encompassed constant force amplitude  $\Delta F$ , constant stress intensity amplitude  $\Delta K$ , and stress intensity threshold  $\Delta K_{th}$  testing. Constant  $\Delta F$  tests were carried out to obtain the Paris parameters. Preliminary testing was used to establish workable  $\Delta K$  ranges that would result in a linear Paris relationship. All tests were undertaken with an R ratio of 0.1. A complimentary constant  $\Delta K$  testing programme was carried out to isolate the effect of material heterogeneities on the measured FCGR.  $\Delta K$  values were set to  $20 \text{ MPa} \cdot \text{mm}^{0.5}$ . For this purpose, two R ratios were used (0.1 and 0.5) to distinguish the effect of increased loading. Both constant  $\Delta F$  and constant  $\Delta K$  testing programmes were carried out at a loading frequency of 15 Hz. A final test programme involved the determination of the  $\Delta K_{th}$  through a decreasing  $\Delta K$  approach. This was achieved by maintaining  $K_{MAX}$  constant and gradually increasing  $K_{MIN}$ . The decreasing  $\Delta K$  rate was determined by the same relationship as the one stated on Eq. (1). An initial R ratio of 0.5 and C value of  $-0.4 \text{ mm}^{-1}$  were used for this purpose.  $\Delta K_0$  was set at  $14 \text{ MPa} \cdot \text{mm}^{0.5}$  and  $\Delta K$  was adjusted every 0.1 mm of crack increment, until no increment was measured after  $1 \times 10^6$  cycles.  $\Delta K_{th}$  and the Paris parameters  $\log_{10}(C)$  and  $m$  were finally determined by the procedure set by Ohta *et al.* [34].  $\Delta K_{th}$  testing was carried out at a loading frequency of 60 Hz. All test experiments were repeated 3 times per material and specimen orientation, except were indicated.

### 2.3. Fractography, microscopy and crystallography

Optical microscopy was carried out using a Keyence VHX-600 microscope under epi illumination. Standard specimen preparation was used for metallographic inspection. Etching was done through submersion with 5 % Nital to reveal microstructural features within the HSLA steel; Kalling's No. 2 etchant was used to visualize interdendritic ferrite, carbides, and oxides on the ASS portion. For bi-material specimens, etching was carried out under a two-step etching by swabbing.

Fractographic analysis was carried out to establish a correlation between the specimen's features and the measured fatigue crack propagation behaviour. After fatigue testing, the bi-material and HSLA steel specimens were cooled with liquid nitrogen, cracked open through 3-point bending, and brought back to room temperature through subsequent submersions in water and isopropanol alcohol. The latter step was done to minimize the effect of corrosion during de-frosting. AS steel specimens were heat-tinted at  $350 \text{ }^\circ\text{C}$  for 15 min. and cracked open. Macroscopic imaging of the fracture surfaces was carried out with an optical microscope Keyence VHX-700. Partial illumination (quadrants top and left) was used to accentuate fracture features. Features like the

crack extension after pre-fatigue  $a_p$ , the position of the bi-material dissimilar fusion line  $Z(BM)$ , and the crack extension after test completion  $a_f$  were obtained as an average of 5 measurements equally spaced across the full width of each specimen. Scanning electron microscopy of the fracture surfaces was done with a JEOL JSM-IT100 InTouchScope<sup>TM</sup> instrument at an accelerating voltage of 20 kV.

Fractography is complimented with crystallographic analysis of the crack flanks to better understand the crack propagation process. Standard metallographic sample preparation was used with a final polishing step in colloidal silica (OPS) for a minimum of 30 min. Electron backscatter diffraction (EBSD) mapping was carried out with a FEI® SEM-Quanta FEG 450 SEM from ThermoFischer Scientific with an integrated EDAX detector. An accelerating voltage of 20 kV and a current of 13nA was used for all mapping purposes. Mapping step sizes are indicated in the caption under each figure in the results and discussion sections. Post-processing was done with the EDAX OIM Analysis software v8.6. Martensite variant analysis was performed to distinguish between deformation-induced and allotropic martensite. EBSD maps obtained with a step size of  $0.1 \text{ } \mu\text{m}$  about the crack flanks of two different specimens were cropped and coarsened. This was done to avoid noise derived from mis-indexed points across the crack void, and to reduce computational load. Variant and packet identification was carried out with the open-source MATLAB toolboxes MText and ORTools, following the grain graph procedure. A step-by-step procedure is explained in detail elsewhere [35]. In every case, the parent phase was considered face-centred cubic and the child phase body-centred cubic. The re-construction of Parent Austenite Grains (PAG's) was carried out assuming a Kurdjumov-Sachs (K-S)  $\{111\}_\gamma \parallel \{110\}_{\alpha'}$  and  $\langle 110 \rangle_\gamma \parallel \langle 111 \rangle_{\alpha'}$  orientation relationships (OR).

Lastly, Transmission Kikuchi Diffraction (TKD) was used to establish the relationship between the martensite lath orientations and the fatigue fracture plane. Specimen preparation involved the conventional lift out method of electron-transparent lamella with a xenon plasma focused ion beam Helios G4 PFIB UXe. To avoid ion milling of the fracture features at the region of interest, beam-induced platinum deposition was used. After ion milling and polishing, the lamellae were inspected under scanning transmission electron microscopy (STEM) at 30 kV. Subsequently, specimens were tilted  $40^\circ$  from horizontal and mapped with transmission-EBSD (t-EBSD). Mapping was done with a step size of  $0.01 \text{ } \mu\text{m}$  for this purpose.

## 3. Results

### 3.1. Constant force and near-threshold FCGR

The results obtained from constant  $\Delta F$  fatigue testing and  $\Delta K_{th}$  experiments are presented together on Fig. 3-1. On this figure, all data obtained above  $15 \text{ MPa} \cdot \text{m}^{0.5}$  belongs to the constant  $\Delta F$  experimental programme, whereas the data obtained for lower  $\Delta K$  values are obtained from the near  $\Delta K_{th}$  programme. For ease of representation, data is binned every  $2.5 \text{ MPa} \cdot \text{m}^{0.5}$  along the linear Paris regime and every  $0.5 \text{ MPa} \cdot \text{m}^{0.5}$  in the near  $\Delta K_{th}$  regime. Error bars at each data point indicate one standard deviation. The results obtained from the regression analysis proposed by Ohta *et al.* [34] are shown graphically for the joint  $\Delta K_{th}$  and  $\Delta F$  data, with 90 % confidence interval bands.

As indicated on the figure legend, the data on Fig. 3-1 is distinguished by material and the specimen orientation. Fig. 3-1 (a-b) show the data obtained for AS steel mono-material specimens; Fig. 3-1 (c-d) from bi-material specimens; and Fig. 3-1 (e-f) for HSLA-steel specimens. The regression results per material are shown together on Fig. 3-1 (g-h) for ease of graphical comparison. Fig. 3-1 (c-d) show results for bi-material specimens containing also data shown in blue and yellow, as these data points were measured across the un-diluted regions of the bi-material specimens. However, all regression values are reported only for points belonging to the interface. The reader is referred to the web

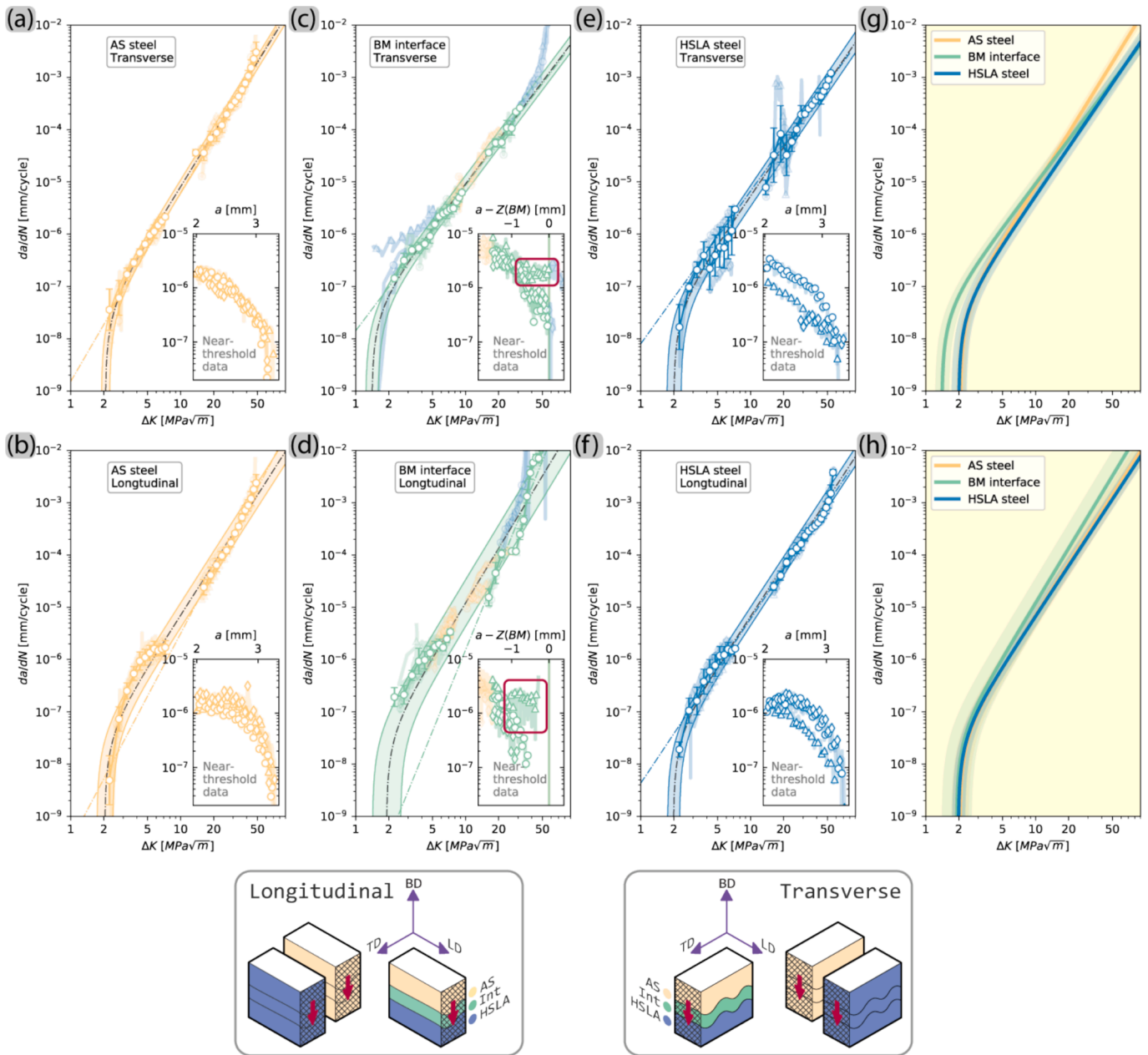


Fig. 3-1. Near-threshold and Paris regimes for SENB samples for (a-b) AS steel specimens, (c-d) bi-material specimens and (e-f) HSLA steel specimens. (g) and (h) show per orientation the regression results and 90% confidence interval bands stacked for all three material conditions.

version of this publication to access the illustrations with the intended colours. Tabulated results of the regression analysis are shown in Table 3-1.

Mono-material specimens show overall consistent results. The mono-material AS steel and the mono-material HSLA steel results show overall good agreement with the regression analysis. Also, the regression values

Table 3.1

Regression parameters for Paris regime and  $\Delta K_{th}$  values. Regression values solely obtained from the Paris regime are shown between brackets  $\pm$  standard error.

	Transverse specimen orientation			Longitudinal specimen orientation		
	$\Delta K_{th}$	m	$\log_{10}(C)$	$\Delta K_{th}$	m	$\log_{10}(C)$
	$MPa \cdot m^{0.5}$	$\log_{10}(\text{mm/cycle})$ $\log_{10}(MPa \cdot m^{0.5})$	$\log_{10}(\text{mm/cycle})$	$MPa \cdot m^{0.5}$	$\log_{10}(\text{mm/cycle})$ $\log_{10}(MPa \cdot m^{0.5})$	$\log_{10}(\text{mm/cycle})$
AS Steel	2.07	3.40 (3.61 $\pm$ 0.03)	-8.49 (-8.82 $\pm$ 0.04)	2.04	3.28 (3.97 $\pm$ 0.02)	-8.43 (-9.48 $\pm$ 0.03)
BM interface	1.40	2.79 (2.78 $\pm$ 0.13)	-7.83 (-7.85 $\pm$ 0.15)	1.90	3.47 (5.17 $\pm$ 0.09)	-8.39 (-10.98 $\pm$ 0.13)
HSLA steel	2.00	3.08 (2.92 $\pm$ 0.06)	-8.34 (-8.10 $\pm$ 0.09)	1.99	3.20 (3.15 $\pm$ 0.02)	-8.37 (-8.37 $\pm$ 0.03)

show negligible differences between the different orientations, suggesting no relevant anisotropy in terms of fatigue crack propagation. Nevertheless, Fig. 3-1 (b) shows a higher degree of dispersion for the data points obtained in the near  $\Delta K_{th}$  specimens. This could be attributed to the R ratio effect and is discussed in detail in section 4.1.2. Moreover, Fig. 3-1 (e) shows an important degree of dispersion across the higher  $\Delta K$  values for the transverse HSLA steel specimens. These features are related to process-induced defects, mostly consisting of lack of fusion. These defects are presented in greater detail in section 4.1.3.

Bi-material specimen results contrast from their mono-material counterparts through a few important features. Both the transverse and longitudinal results show higher dispersion than their mono-material counterparts. The source of this dispersion appears to be twofold. First, on Fig. 3-1 (d) a large dispersion in FCGR is measured for the highest  $\Delta K$  values. If Paris parameters are derived solely from the data obtained in this regime, the results suggest a very high sensitivity to  $\Delta K$ , much higher than the mono-material counterparts. This is easily appreciated by the  $m$  values presented between brackets in Table 3-1. Second, in both transverse and longitudinal directions, the near- $\Delta K_{th}$  data shows strong discrepancies between different specimens. Inserts in all subfigures show the measured crack propagation rate as a function of crack length. For mono-material specimens, a clear decreasing tendency is observed. On the bi-material specimens, nonetheless, some specimens show decreasing FCGR as they approach  $Z(BM)$ , but certain specimens do not. Although the stress intensity amplitude is consistently decreased, the crack propagation rate re-accelerates as the crack front approaches  $Z(BM)$ . This phenomenon is highlighted in red on the inset figures in Fig. 3-1 (e) and Fig. 3-1 (d). To better distinguish this phenomenon, it is best to isolate it under constant stress intensity and R ratio parameters. This is done in the following section.

### 3.2. FCGR under constant $\Delta K$

To clearly distinguish the effect that the interface might impose on FCGR across the bi-material specimens, constant  $\Delta K$  experiments are carried out. Fig. 3-2 shows the results for this fatigue testing programme, distinguishing data based on material condition, orientation, and R ratio. In this case, FCGR results are shown binned every 0.25 mm of crack extension. Error bars on each point show a single standard deviation, as obtained from the binning process. Bi-material crack extension results are normalized to the position of the interface, where negative values show data points measured on the undiluted AS steel and interface layers, and positive values belong to points measured across  $Z(BM)$  and into the HSLA steel layers. Average values are shown as a dotted line alongside 90 % confidence interval bands. For the bi-material specimens, only data belonging to the interface layer is considered for statistical analysis. Numerical results are shown in Table 3-2.

Under a constant  $\Delta K$  loading scheme, a clearer relationship can be established between the different materials and their individual response to crack propagation. For a given specimen orientation and R ratio, AS steel typically shows higher crack propagation rates than HSLA steel. In every case, R ratios of 0.5 result in higher growth rates than their 0.1 R ratio counterparts. A slight difference is appreciated between the transverse and longitudinal specimens, typically leading to marginally higher fatigue crack growth rates for longitudinal specimens. Nonetheless, this difference lies within the range of the estimated measurement error. Dispersion of the HSLA steel data is attributed to the lack of fusion defects. These have a more noticeable and adverse effect when the crack lies on the BD-LD plane (transverse specimens). These defects are described in detail in section 4.1.3. None of the mono-material test results indicate a periodic effect that could be related to microstructural differences between the root and the top of each material layer. This indicates that for practical purposes in terms of fatigue crack resistance the mono-material specimens are homogeneous across their layers.

Distinctively, the interface layer shows a variable resistance to crack

growth as a function of the position. Bi-material specimens show a clear tendency to decelerate crack propagation as the crack front progresses. The position of the lowest measured average growth rates is indicated with a red marker on Fig. 3-2 (b, e, h, k). The crack deceleration is most notorious on the transverse specimens under an R ratio of 0.1. These specimens show an average  $\Delta$  in crack propagation rate of  $-6.10E-05$  mm/cycle ( $-0.77 \log_{10}$  steps), when compared to the average propagation rate of the preceding AS steel layers. This tendency is less pronounced but common for the rest of R ratios and specimen orientations.

As the crack approaches  $Z(BM)$ , the deceleration effect is lost. The highest average rate change is measured on the transverse-oriented specimens at a loading ratio of 0.5, where a  $\Delta$  of  $+3.20E-04$  mm/cycle ( $+0.75 \log_{10}$  steps) was observed. This entails propagation rates almost an order of magnitude higher reached within a crack propagation length of  $\sim 1$  mm. Growth rates subsequently slow down as the crack front crosses the dissimilar fusion line.  $Z(BM)$  is thus the position at which highest rates are measured. This is not immediately clear in all specimens, as lack of fusion defects populate the HSLA steel material volume across many specimens. Nonetheless, this trend is consistent with all material groups in all orientations and R ratios, typically showing the most pronounced effect on transverse-oriented specimens with higher R ratios.

Constant  $\Delta K$  is ensured through the calibration of  $\Delta K$  as a function of the elastic moduli and the position of the bi-material interface, as stated in Eq. (3) in the method section. Assuming that the calibration is sufficient to control this experimental procedure, the deceleration and acceleration effects may be attributed to the microstructural constitution of the interface *in-lieu* of the macroscopic effect derived from mismatching elastic moduli. Thus, a closer look is taken into the fracture features in section 3.3 and the microstructural constitution of the three material volumes in section

### 3.3. Fractography

To establish a relationship between the measured fatigue crack growth rates and the geometrical features of the specimen, macroscopic fractography is carried out. For each specimen, the position of the crack front by the end of the pre-fatigue procedure  $a_p$ , the position of  $Z(BM)$ , and the position of the crack by the end of the fatigue test  $a_f$  are highlighted in Fig. 3-3. Both fracture surfaces are shown for each specimen. Two reference specimens are shown in Fig. 3-3 (a) and Fig. 3-3 (b), to highlight the differences in geometry of the interface layer on the crack plane; Fig. 3-3 (c) and Fig. 3-3 (d) provide examples of the location and geometry of the lack of fusion defects cited in sections 3.1 and 3.2. The measured FCGR as a function of crack position are shown for every specimen presented and approximately scaled to fit between the average position of  $a_p$  and  $a_f$ .

Differences on the appearance of the fracture surface are attributed to the different material regions and load levels. Crack initiation at the notch is typically achieved with large  $\Delta K$  values. As the crack approaches  $a_p$ , the  $\Delta K$  values are reduced to a level below the one intended to start the fatigue test, effectively reducing the plastic work imposed on the AS steel material. This is reflected on the four samples shown on Fig. 3-3, where a distinctly faceted fracture geometry populates the region adjacent to the notch. These facets become less apparent as the crack progresses up to  $a_p$ , and across the rest of the AS steel material volume. The crack then crosses into the interface layer, developing distinct fracture features. The large facets in the AS steel are less apparent, giving place to a predominantly flat surface. Faint facets are however still perceivable. As the crack crosses the dissimilar fusion line into the HSLA steel layers, the fatigued fracture surface becomes duller, and features become unperceivable at a macroscopic scale. The surfaces corresponding to final tearing beyond  $a_f$  fracture show tortuous detachment, characteristic of HSLA steel alloys.

Microscopic characterization of the fracture surface provides

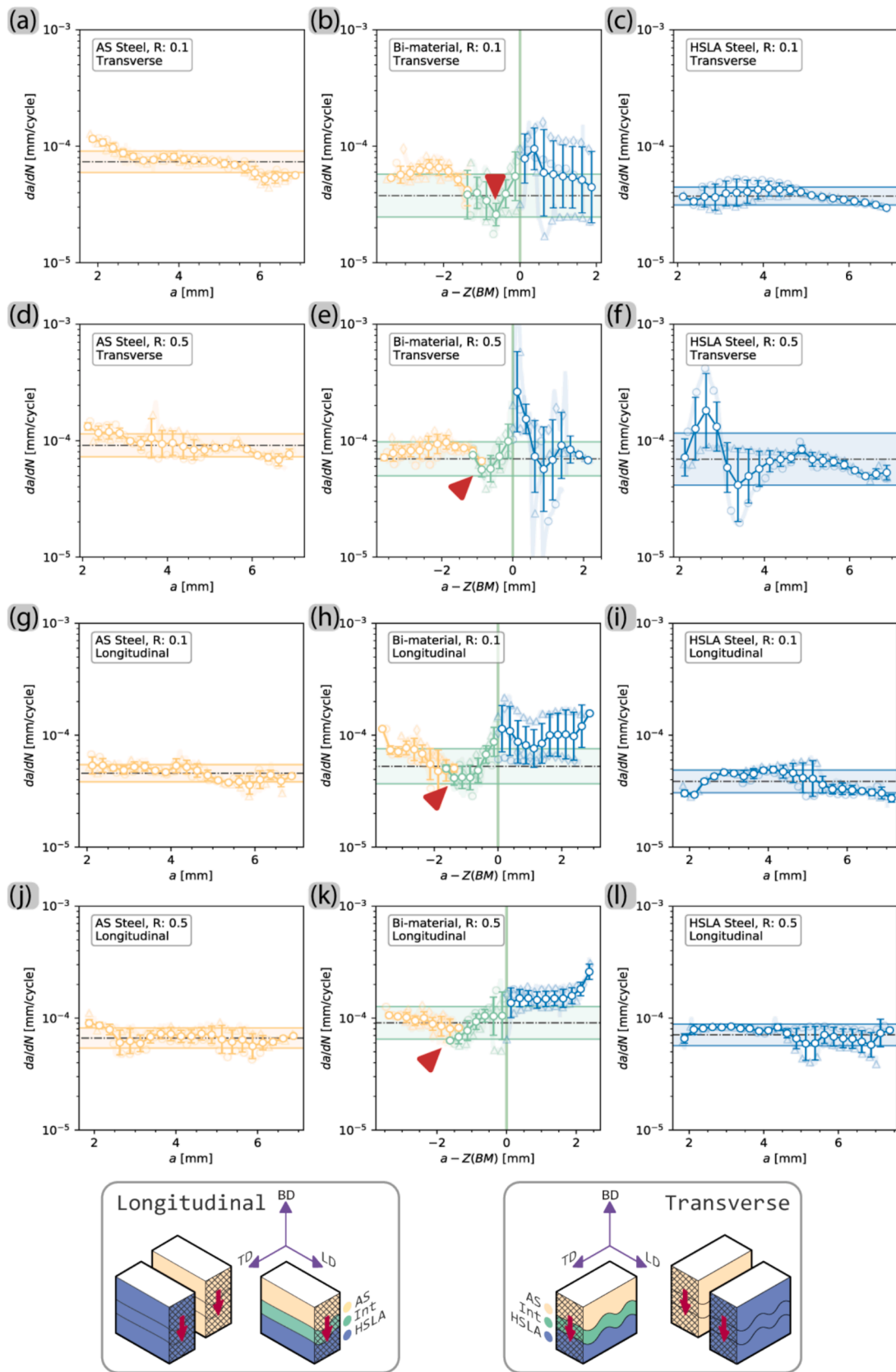


Fig. 3-2. Constant  $\Delta K = 20 \text{ MPa}\cdot\text{m}^{0.5}$  crack propagation rates for (a, d, g, j) AS steel specimens, (b, e, h, k) bi-material specimens and (c, f, i, l) HSLA steel specimens. For bi-material specimens, the position of the crack front is normalized to the position of the dissimilar fusion line, such that  $a - Z(BM) = 0$ .

**Table 3.2**

Average fatigue crack propagation rates as a function of R ratio, material condition and orientation. All data is provided as  $\log_{10}$  (mm/cycle)  $\pm$  one standard deviation.

	Transverse specimen orientation		Longitudinal specimen orientation	
	R 0.1	R 0.5	R 0.1	R 0.5
AS steel	$-4.134 \pm 0.09$	$-4.041 \pm 0.10$	$-4.339 \pm 0.08$	$-4.178 \pm 0.09$
BM interface	$-4.424 \pm 0.19$	$-4.156 \pm 0.15$	$-4.277 \pm 0.16$	$-4.042 \pm 0.15$
HSLA steel	$-4.428 \pm 0.22$	$-4.159 \pm 0.22$	$-4.412 \pm 0.10$	$-4.150 \pm 0.10$

detailed insights on the different mechanisms controlling crack

propagation. Fig. 3-4 (a) and (b) show low magnification features of two different samples, used to provide context to the features observed on Fig. 3-4 (c-h). The macroscopic facets observed on the AS steel fracture surface are shown under high magnification in Fig. 3-4 (c). The faces of these facets are populated by densely packed tearing features related to ductile mixed-mode fracture. Indications of striations across this material volume are not clear. Orange markers indicate locations where secondary cracks are identified. Although most of the fracture surface across the AS steel volume shows similar traits, the region on the vicinity of the fusion line shows occasionally distinct features. The red marker on Fig. 3-4 (d) indicates a band of transgranular cleavage combined with tearing fracture, most resembling the mixed fracture modes observed across the interface layer shown on Fig. 3-4 (e) and Fig. 3-4 (f). This feature most likely originates from unmixed material as obtained during deposition.

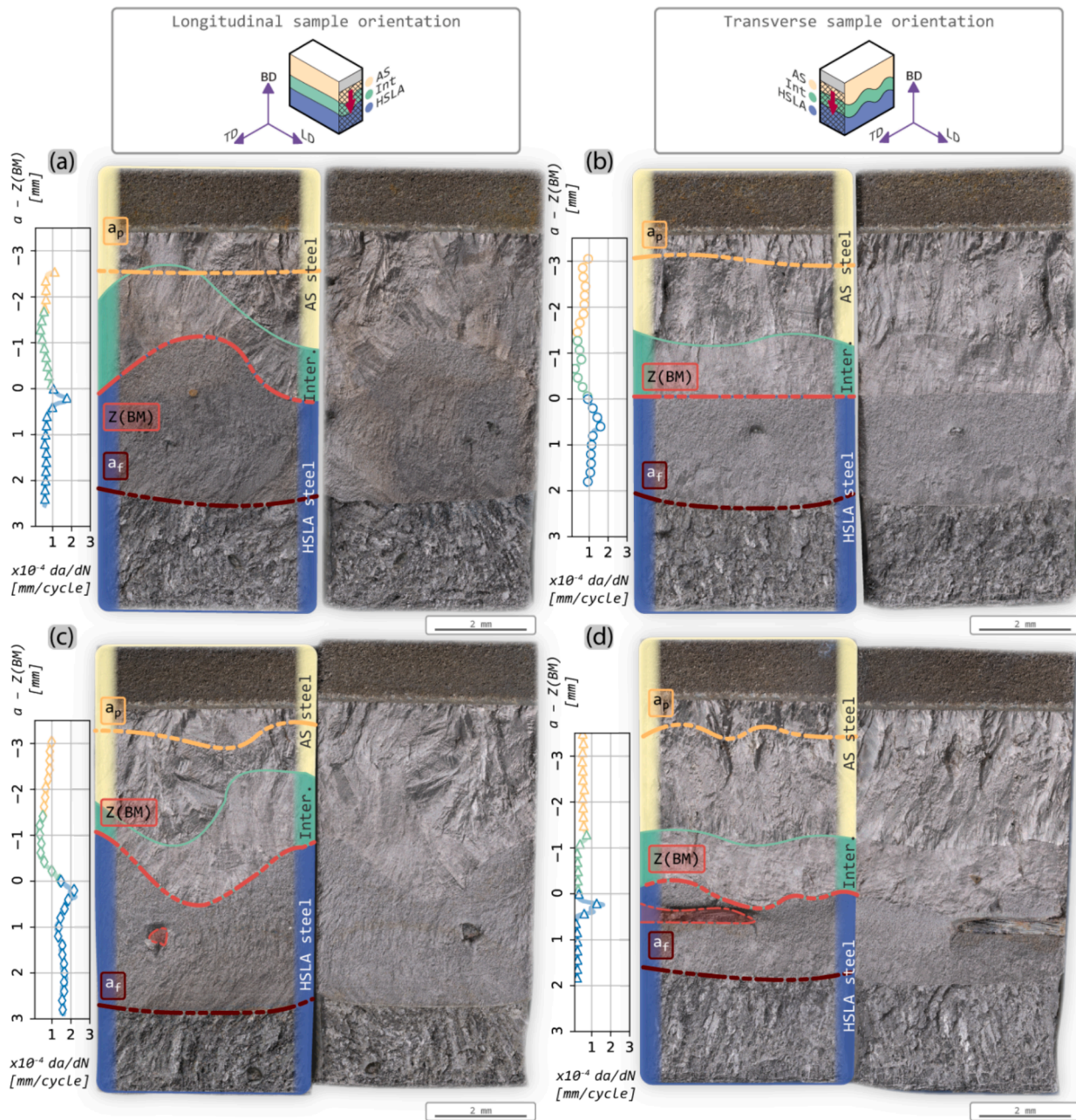


**Fig. 3-3.** Typical macroscopic fracture features of selected specimens, as observed under optical microscopy. Samples were tested under a constant stress intensity range of  $\Delta K$ :  $20 \text{ MPa}\cdot\text{m}^{0.5}$  and R: 0.1. Fracture surfaces are presented alongside their corresponding measured fatigue crack propagation rates. (a) and (b) show typical features for longitudinal and transverse oriented samples. (c) and (d) show location of lack-of-fusion defects within the HSLA steel material volume.

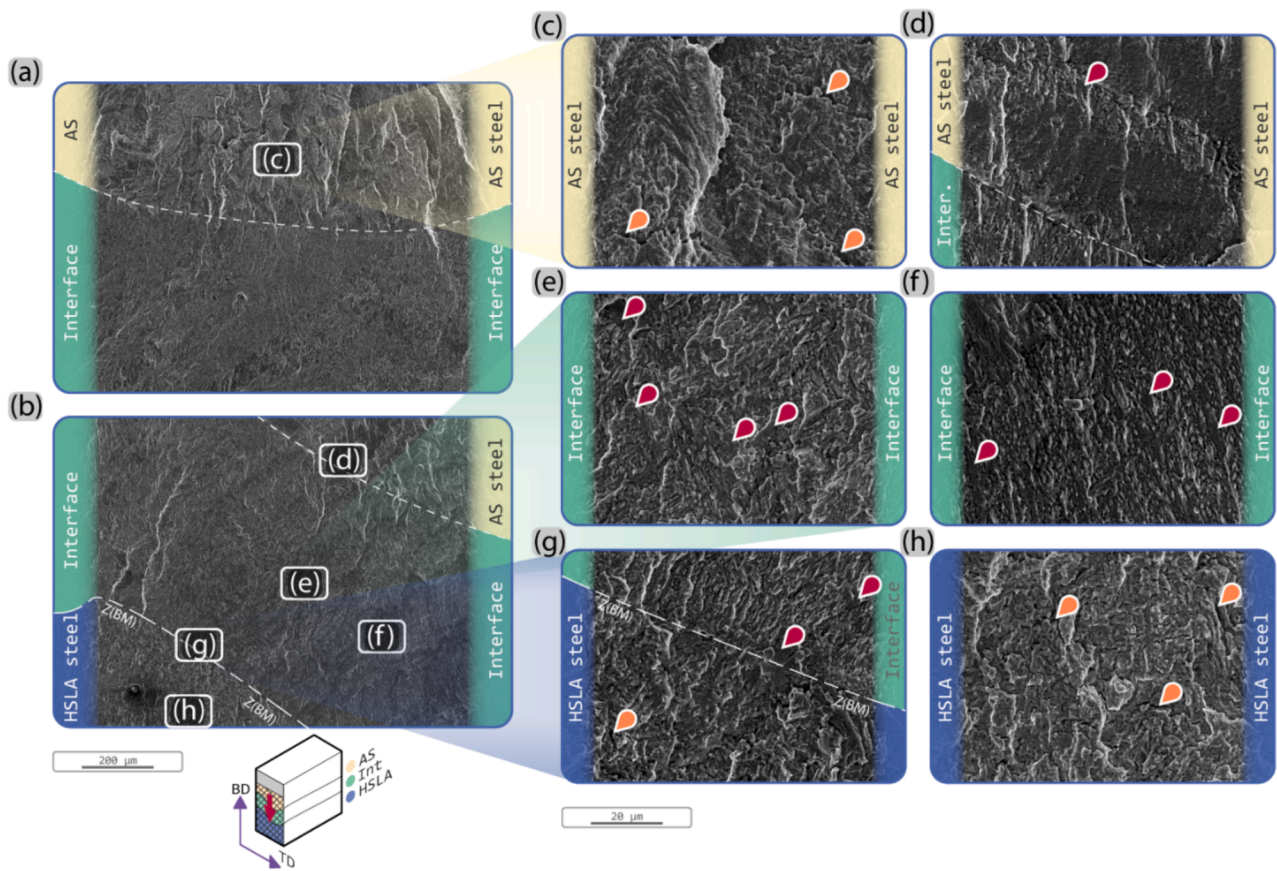


**Fig. 3-4.** Fracture features as observed under scanning electron microscopy. (a) and (b) show a general overview of the regions of interest under low magnification, and specific location of the features shown on (c-h).

Having established the features typically observed across the AS steel layer, it is simpler to identify how unique the fracture features are across the interface layer. At the interface layer, the transformation of metastable austenite into martensite makes itself apparent across the fracture surface features. Fig. 3-4 (e) and Fig. 3-4 (f) show transgranular cleavage combined with tearing traits obtained from the fracture of martensite. The features on Fig. 3-4 (f) converge neatly in a single orientation, whereas the location shown on Fig. 3-4 (e) shows tear traits in a multitude of orientations. The origin to this difference can be attributed to the combination of two factors: load direction and the crystal orientation of the grain being fractured. This is discussed in depth in section 4.2.3. Markers on Fig. 3-4 (e) and Fig. 3-4 (f) indicate the location of small cleavage surfaces. At  $Z(BM)$ , in line with the features observed in Fig. 3-4 (e) and Fig. 3-4 (f), shows combined transgranular cleavage and tear fracture, with tear features neatly oriented together. These features are shown in Fig. 3-4 (g) and fit with the location of the band of martensite typically formed along this dissimilar fusion line. The red markers show the location of cleavage surface. Across  $Z(BM)$ , a tearing topography surface is obtained from the HSLA steel layers. This accompanied by secondary cracks (orange markers).

### 3.4. Microstructural characterization

The fracture features in the previous section suggest a connection between the microstructure and the mechanisms controlling crack propagation. Hence, this section is dedicated to the microstructural characterization of the bi-material specimens before and after fracture.

In first instance, the microstructural constitution of the undiluted AS steel and HSLA steel are presented to easily distinguish microstructural nuances in the diluted interface layer before deformation. On one hand, Fig. 3-5 (a) presents the microstructure of the undiluted AS steel

observed on three different planes after etching. Austenite populated by vermicular ferrite is observed across the bulk of this material volume, although interdendritic and intercellular ferrite are occasionally observed at the fusion line between subsequent layers. Ferrite content amounts to about 4.7 % of the surface area mapped on Fig. 3-5 (b) and Fig. 3-5 (c), as measured by the EBSD phase mapping. Grain sizes across this material volume range from 100  $\mu\text{m}$  and up to millimetres in length. On the other hand, Fig. 3-5 (g) shows the etched microstructure of HSLA steel. This material volume is in large constituted by interlocking laths, commonly denominated as acicular ferrite. The acicular ferrite observed is in turn is composed by combined phase fractions of bainite and Widmanstätten ferrite, alongside dispersed oxides. A minor phase fraction of idiomorphic ferrite is also identified, delimiting parent austenite grain boundaries. The grain boundaries of the acicular ferrite are highlighted on Fig. 3-5 (h) through IQ mapping. The grain size across the HSLA steel amounts to an average of  $1.35 \pm 0.15 \mu\text{m}$ . Fig. 3-5 (i) shows that this material volume is practically constituted solely by bcc constituents. However, unlike comparable HSLA steel weld metal deposits [36], there is no indication of martensite nor pearlite. Dedicated studies on the deformation mechanisms and fracture are available for comparable AS steels [37,38] and HSLA steels [39,40]. Hence, the presentation of results here onward concentrates on the interface layer.

Due to the mixing of the two parent alloys, the interface layer presents unique features distinct from the parent materials. Fig. 3-5 (d) shows the microstructural features at and about the interface layer after a two-step etching process. The dominant phase constituent is austenite, representing about 60 % of the surfaces inspected. The remaining 40 % are bcc phases, in large represented by ferrite and occasionally martensite. Some microstructural heterogeneities are however easily recognizable by the heterogeneous occurrence of etched ferritic phases. Under optical microscopy these phases are only partially etched, but

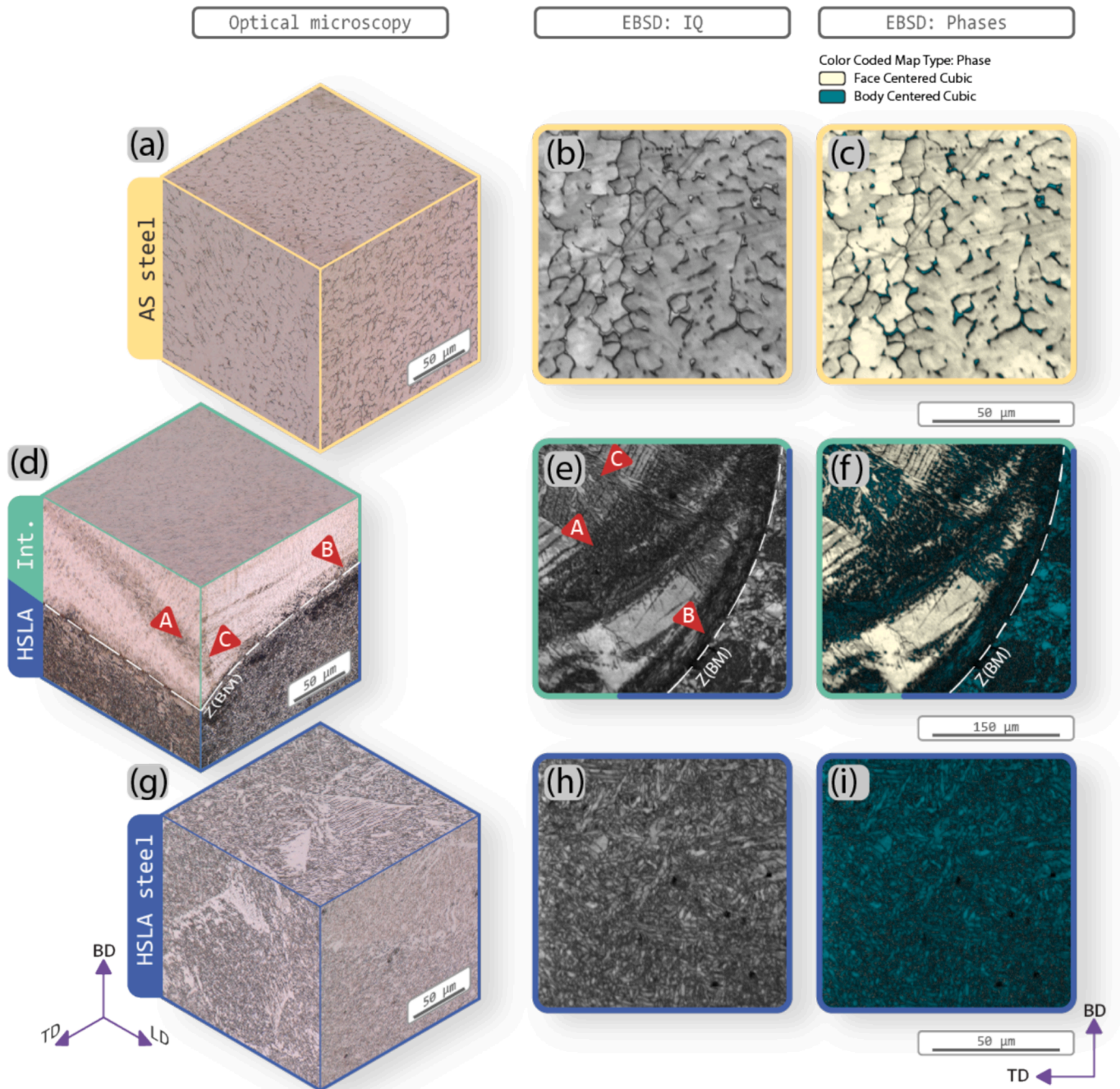


**Fig. 3-5.** Optical microscopy, EBSD image quality (IQ) and phase maps of undeformed material for (a – c) AS steel, (d – f) the interface, and (g – i) the HSLA steel material volumes. EBSD mapping was carried out with a step size of 10 nm for (a-b), and 70 nm for (e-f) and (h-i). Note: the magnification of maps (e-f) is 3 times lower than that of the (b-c) and (h-i) maps..

they are clearly distinguishable through IQ maps in Fig. 3-5 (e) and phase mapping in Fig. 3-5 (f). Firstly, marker A in Fig. 3-5 (d) and Fig. 3-5 (e) show a ferrite and martensite band originating from inhomogeneous mixing of the AS steel weld metal and the previously deposited HSLA substrate. Secondly, marker B shows a second instance of martensite in the form of a band found intermittently along the dissimilar fusion line. Lastly, marker C shows the location of disperse primary ferrite. Across the interface, austenite commonly forms grains of about 300 μm in size, while the ferrite phase fraction may range between individual particles of 10 μm in diameter, or larger networks of primary ferrite of several hundred microns wide. The latter ferrite networks are most easily recognizable along islands or bands, like the one indicated

by markers A and C. A more in-depth presentation of the microstructural features found across the undeformed interface layer is provided in a related publication [29].

Although austenite represents the largest phase fraction across the interface layer, the fracture surface features presented in section 3.3 do not correspond to those of an austenite matrix. On the contrary, the fracture features found across this region suggest that the crack propagated solely across martensite. A practical approach to confirm the presence of martensite is through microstructural inspection of the deformed specimens. For this purpose, two different samples were chosen. Fig. 3-6 shows the image quality (IQ) and phase maps of two samples tested under constant  $\Delta K$ . The difference between both samples

lies on the R ratio, namely 0.5 for Fig. 3-6 (a-d) and 0.1 Fig. 3-6 (e-h). Fig. 3-6 (a) and Fig. 3-6 (e) show the IQ maps under low magnification. Since the maps are obtained from arbitrary planes across the sample, a considerable difference in size of the interface can be appreciated. This is simply due to the varying geometry of the interface. IQ maps are useful to characterize the degree of clarity with which Kikuchi patterns are obtained. The quality of such patterns can be attributed to different factors including sample preparation, mapping parameters, dislocation density and crystal deformation, between others. Given that sample preparation was carefully performed, and the mapping parameters consistent, the changes in grayscale can most likely be attributed to the degree of crystal defects: large crystals without appreciable deformation appear lighter, while regions with a high density of crystal imperfections and grain boundaries appear darker. In this case, martensite appears dark due to its high dislocation and grain boundary density [41].

Fig. 3-6 (a) shows the crack flank region of a specimen with low amount of disperse ferrite banding across the interface layer. The grains thus appear mostly clear, except for a band of martensite along the fusion line pointed with a green marker, and a band of ferrite on the upper region of the interface. Fig. 3-6 (b) through (d) show that although the material volume surrounding this region is mainly undeformed, the locations closest to the crack flanks have indeed transformed into martensite. Distinction of ferrite and martensite is not possible simply through phase mapping, but it is understood that most of this mapped bcc phases are bcc' instead based on the grain morphology and the lack of ferrite in their vicinity. The map in Fig. 3-6 (b) shows the boundary between the diluted interface and the undiluted AS steel layer. Only the map shown on Fig. 3-6 (d) includes the martensite band at the fusion line and the idiomorphic ferrite formed immediately beneath it.

Fig. 3-6 (e) offers a contrasting example. The map shows a dense ferrite population, with three clear bands of very low IQ values across the interface layer and an additional band along the fusion line. These are shown with green markers. Under higher magnification, it is easier to confirm the martensitic nature of these low IQ bands. Phase maps shown in Fig. 3-6 (g) and Fig. 3-6 (h) help identify this phase constituent to be martensite based on the grain morphology and size. The location shown in Fig. 3-6 (h) also provides evidence of appreciable crack deflection. The map on Fig. 3-6 (f) shows a clear example on this cut plane of martensite obtained from the TRIP effect of metastable austenite. Although this location is found within the undiluted AS steel, an intrusion of the underlying interface layer can lead to local regions of metastable austenite. This matches the observation made on Fig. 3-4 (d).

The appearance of martensite across the interface has been presented by us in a related publication [29]. Nevertheless, the effect that the martensite had on the crack propagation process is to be further discussed, both in terms of crack propagation speed and orientation. This is done in detail in the following section.

#### 4. Discussion

The results of this work show that fatigue behaviour of this 3D-printed bi-material structure is affected by a complex interplay between macroscopic and microscopic effects, where behaviour of interface layer is of most interest. At a macrostructural scale, the fatigue crack growth rates across the interface show a unique behaviour compared to the parent materials. Crack retardation at the top of the interface layer is consistently accompanied by crack acceleration as the crack front approaches the dissimilar fusion line  $Z(BM)$ . Changes in specimen orientation and R ratio are also shown to cause measurable differences. These phenomena are discussed in detail in section 4.1.

The uniqueness of the interface layer is confirmed at a microstructural scale. Fracture surface analysis demonstrates that there is a fundamental difference between the undiluted and the diluted stainless steel material volumes. This observation is supported by EBSD analysis, where the crack front is demonstrably accompanied by martensite throughout the entire width of the interface layer. The interplay

between the previously formed allotropic martensite and deformation-induced martensite is interesting and may help clarify the dual competing effect of deceleration and acceleration at the interface. Microstructural aspects on fatigue crack growth are discussed in detail in section 4.2.

#### 4.1. Macrostructural aspects on FCG at the interface

##### 4.1.1. The dissimilar interface effect

Contrary to what was expected, in this work we observe an initial crack retardation followed by a discernible crack acceleration because of a plastically mis-matched interface. This observation does not agree to what would have been expected from a perfectly joint plastically mis-matched bi-material structure. Suresh *et al.* [42] propose that dislocation emission from the crack tip is restricted by the harder material, obstructing cyclic slip and therefore obstructing fatigue crack growth. The authors confirmed their results experimentally in a later study [43]. Pippin and Riemelmoser [44] made a similar observation through their numerical analysis, indicating that crack tip opening displacement gradually decreases as the crack approaches the dissimilar fusion line. The authors point out that crack closure effects should become more predominant as the crack front transits from the softer to the harder material, leading to retardation in crack propagation. Work by Jian *et al.* [45] agrees with this observation experimentally. The authors draw this conclusion from a mild steel and AS steel bi-material joint obtained through explosive cladding. The results obtained from our work under constant  $\Delta K$  testing in this work show nevertheless an opposite trend.

The variable FCGR across the interface must be thus attributed to its heterogeneous microstructure. The dilution of the AS steel alloy on the HSLA steel substrate layers leads to an interface layer with a unique chemical and microstructural constitution, as characterized in a related study [29]. In large, the interface layer is formed by a metastable austenite phase populated by a considerable fraction of ferrite [25]. As the metastable austenite deforms, it transforms into martensite to accommodate large plastic strain. Nevertheless, the heterogeneous chemical constitution of the interface layer also leads to certain regions of high martensite start temperature. This material volume is located mostly alongside the fusion line and in the form of islands (as observed from a BD-TD cross section) or bands (as observed from a BD-LD cross section). Thus, a distinction is necessary between the martensite obtained from allotropic transformations, hereon referred to as allotropic martensite, and that obtained from the deformation of metastable austenite at room temperature, hereon referred to as deformation-induced martensite. A correlation can be drawn between the location of metastable austenite, allotropic martensite and the measure fatigue crack propagation rates obtained through  $\Delta K$  experiments. Within the interface layer, the fatigue crack propagation will be mostly controlled by the deformation of metastable austenite and subsequent fracture of deformation induced martensite, while the root of each bead within the layer will be most affected by the presence of allotropic martensite.

##### 4.1.2. R-ratio effect

As observed under constant  $\Delta K$  experiments, higher R ratios have a detrimental effect on the crack propagation rates. These results are presented on Fig. 3-2 and Table 3-2. The physical effect of the R ratio on the fatigue crack growth process is extensively debated, nonetheless. This dependency on R is associated with the crack-closure effect [46], and the compressive and shear stresses derived from metastable austenite transformation [47]. The fracture morphologies presented on Fig. 3-4 could be explained at least in part because of crack closure, most evident across the fracture surface of the AS steel and HSLA steel layers. Evidence presented by various studies [48,49] suggests a nuanced relationship, as quantifying this closure effect is problematic in the presence of material plasticity and non-linear compliance of the testing apparatus.

As an alternative, Kujawski [50] offered an unbiased approach. By

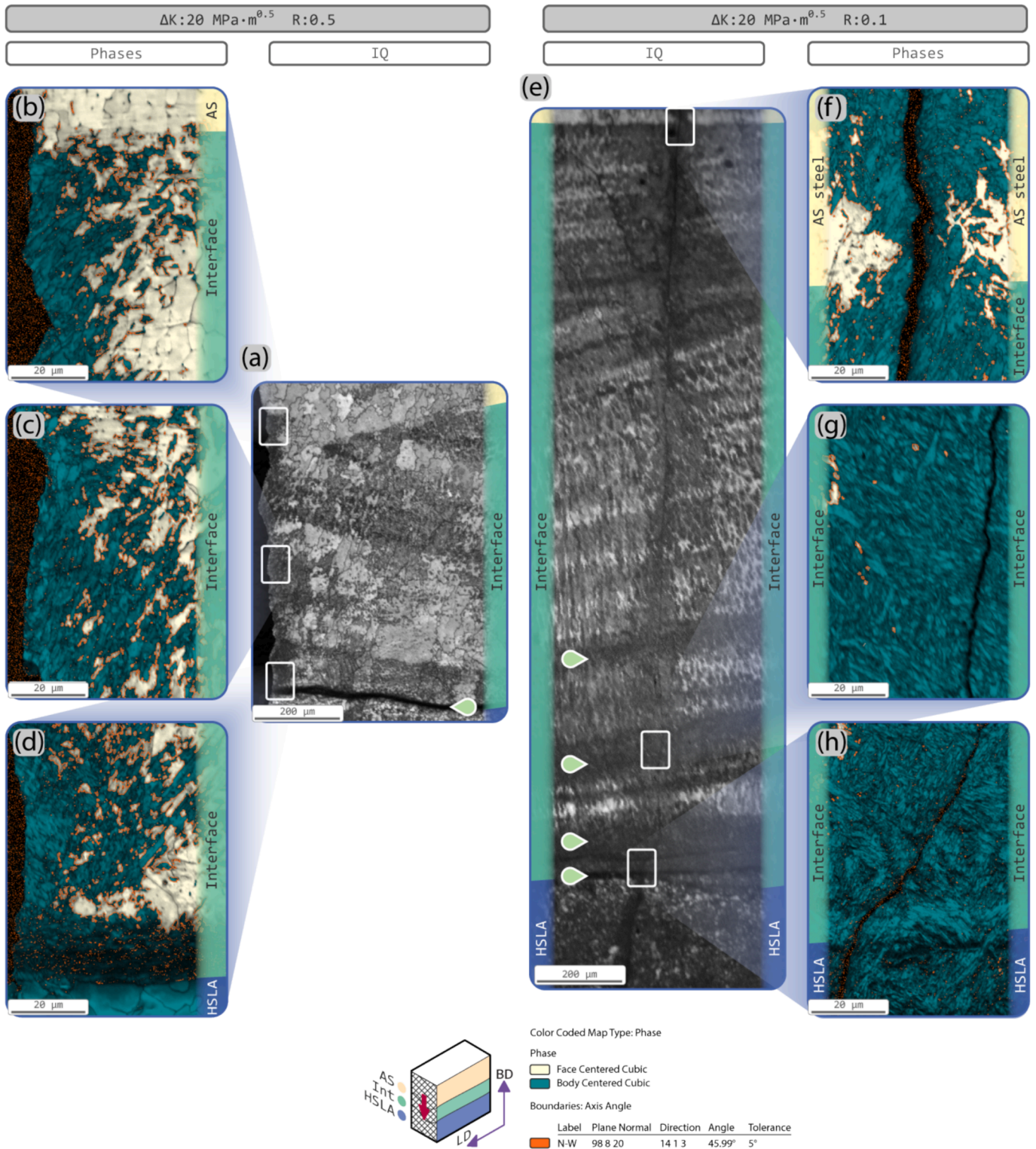


**Fig. 3–6.** EBSD mapping in the vicinity of the crack flank for specimens tested under constant  $\Delta K$ . (a) shows the crack flank of a specimen loaded under an R ratio of 0.5 as an IQ map, alongside detailed phase mapping of regions showing deformation-induced martensite (b, c), and a region combining both deformation-induced and allotropic martensite (d). (e) shows IQ mapping of the interface layer of a specimen tested under an R ratio of 0.1. Detailed phase maps show deformation-induced martensite in (f) and substantial allotropic martensite found across the rest of the interface’s material volume (g, h). Figures (a) and (e) were obtained with a step size of 1.5  $\mu\text{m}$ ; figures (b-d) and (f-h) were obtained with a step size of 0.1  $\mu\text{m}$ . Phase maps show points indexed as bcc in teal and fcc in tan. Due to the locations of the maps, most index bcc points are considered martensite.

means of a normalizing  $K^*$  variable, the FCGR data may be homogenized. The homogenization principle relies on the product of two load parameters, namely  $\Delta K$  and  $K_{MAX}$ , and a material-dependant exponent  $\alpha$ , such that:

$$K^* = K_{MAX}^\alpha \Delta K^{+(1-\alpha)} \tag{6}$$

where  $\Delta K^+$  is the positive part of the applied  $K$  range. This relationship can also be re-stated in terms of R, such that:

$$K^* = \frac{\Delta K^+}{(1-R)^\alpha} \tag{7}$$

The proposed method to obtain the value of  $\alpha$  involves the determination of two set of Paris parameters obtained with two different R ratios. This can be also achieved by estimating the Paris parameters that would fit the measured FCGR data obtained from the constant- $\Delta K$  test. It is done under the assumption that minimal error is incurred if the variation of  $m$  as a function of R [51] is small. The assumption is necessary since  $\alpha$  is obtained by evaluating  $\Delta K$  at a common  $da/dN$  value. The estimated  $\alpha$  parameters, and the resulting  $K^*$  values and the relative error between  $\log \Delta K$  and  $\log K^*$  are presented in Table 4-1.

The approach proposed by Kujawski seems to adequately capture the sensitivity of the materials tested to the R ratio. The highest values of  $\alpha$  are obtained from the material volume most sensitive to  $K_{MAX}$ . In this case, the largest  $\alpha$  exponent is obtained from the bi-material interface layer as measured from transverse-oriented specimens. A high sensitivity of the HSLA material volume to  $\alpha$  is also observed, although this has been attributed to the roughness-induced crack closure [52]. The relative difference between the applied  $\Delta K$  and the estimated  $K^*$  is thus presented in Table 4-1 as relative error in  $\log_{10}$  step. This is done, since FCGR data is assumed to be distributed log-norm. Under  $R = 0.1$ , the relative error between  $\Delta K$  as the  $K^*$  is barely apparent. The relative error incurred under an R ratio of 0.5, though, is more relevant. This is sustained especially for the material conditions most susceptible to the R ratio effect, namely the bi-material interface and the HSLA steel layer (under a constant  $\Delta K$  of 20 MPa·m<sup>0.5</sup>,  $K^* = 25.96$  for the transverse oriented BM interface at an R ratio of 0.5, and  $K^* = 25.35$  for the same orientation and R ratio tested on HSLA steel specimens). Hence, a higher relative induced error is conducive to a more exacerbated R ratio effect.

Previous work has demonstrated a satisfactory relationship between Kujawski's  $K^*$  parameter and the crack growth behaviour in metastable austenite [47,53]. For ductile materials, the crack driving force is mostly affected by  $\Delta K$ , as it is correlated to cyclic damage. On the contrary,  $K_{MAX}$  best correlates to fatigue crack growth of brittle materials as the parameter relates to the applied monotonic damage [50]. Demonstrably, it also correlates closely to TRIP-aided alloys due to the correlation between  $K_{MAX}$  and the size of the process zone ahead of the crack tip. It has been noted previously in this discussion that the deformation-induced martensitic transformation is related to the low stacking fault energy of the interface layer. Thus, a higher dependency of the interface material to  $\alpha$  is expected. The  $\alpha$  parameter serves thus as a quantitative

measure on the sensitivity of  $K^*$  on  $K_{MAX}$ .

#### 4.1.3. Specimen orientation and lack of fusion defects

The different crack planes prove useful to characterize the effect of the interface geometry on the FCGR. Differences in the rate of change in FCGR across the interface can be attributed to the geometry of the layer. Fig. 3-3 (a) and Fig. 3-3 (c) show how much the boundaries of the interface layer may vary across the specimen width. For example, the average position of  $Z(BM)$  on the specimen shown in Fig. 3-3 (a) is at about 4.5 mm from the notched surface, whereas its position varies within a range of 1.3 mm. This in turn is related to more nuanced changes in terms of FCGR. For the same specimen, a gradual acceleration in FCGR is measured across the interface as it approaches  $Z(BM)$ , developing through a length matching  $\sim 1.3$  mm. Transverse-oriented specimens tend to show clearer changes. The specimen shown in Fig. 3-0.3 (d) is a good example, showing how FCGR decrease sharply after the crack front crosses from the un-diluted AS steel layers into the interface layer. Although it could be reasonable to suspect that the crack may lose considerable straightness as it approaches the dissimilar fusion line, specimens tested under near-threshold loading conditions at the interface show straight cracks compliant with curvature conditions set by ISO 12108 [33].

While transverse specimens provide a clearer picture of the relationship between the geometrical features and the measured FCGR, lack of fusion defects in the HSLA material volume create dispersion in the data that makes it difficult to reliably quantify the actual magnitude of crack acceleration. As a crack approached one of these lack of fusion defects, the growth rates in transverse specimens occasionally spiked as a consequence of the additional stress concentration effect. Specimens shown on Fig. 3-3 (c) and Fig. 3-3 (d) show a similar defect in two perpendicular orientations. Their geometry is close to cylindrical, with their long dimension parallel to LD. They typically measure  $\sim 0.4$  mm in diameter and a few millimetres in length. The clear spike effect on Fig. 3-3 (d) shows the crack acceleration effect during constant  $\Delta K$  testing. These lacks of fusion defects are not intrinsic to the AM of bi-metallic specimens. Careful tuning of the deposition parameters can lead to a fully dense material volume with similarly low heat inputs as the ones used in this study. Alternatively, a detailed approach to address the effect of defects within the context of WAAM of titanium alloys is presented by Biwsal et al. [54]. Regardless of the defect occurrence in our study, the trends in FCGR are comparable across specimens, and the data obtained across the interface layer is considered useful to study further in relation to its crack propagation behaviour.

Limited examples are available in literature addressing this orthotropic effect. Extensive work has been done in this study to characterize the differences between FCGR along the build direction and perpendicular to it. The anisotropy observed in this work is in turn derived from the deposition strategy. Nonetheless, the anisotropy observed may be attributed to the geometrical features of the interface layer. Some parallels can be drawn however with work done on a similar alloy pair. Ayand and Kahraman [19] characterized the mechanical properties of a

**Table 4.1**  
Kujawski  $\alpha$  parameters, estimated  $K^*$  values for  $\Delta K$ -controlled fatigue tests, and relative induced error.

	$\alpha$	$K^*$ (R 0.1)	$\frac{\log K^* - \log \Delta K}{\log K^*}$	$K^*$ (R 0.5)	$\frac{\log K^* - \log \Delta K}{\log K^*}$
	—	MPa·m <sup>0.5</sup>	%	MPa·m <sup>0.5</sup>	%
<b>Transverse specimen orientation</b>					
AS steel	0.107	20.23	0.4	21.54	2.4
BM interface	0.376	20.81	1.3	25.96	8.0
HSLA steel	0.342	20.73	1.2	25.35	7.3
<b>Longitudinal specimen orientation</b>					
AS steel	0.192	20.41	0.7	22.85	4.3
BM interface	0.209	20.44	0.7	23.12	4.6
HSLA steel	0.321	20.69	1.1	24.98	6.9

bi-material wall built by alternating the alloys ER70S-S and 308LSi. By changing the specimen orientation, they observed a clear improvement in fatigue performance through constant load amplitude testing. Fatigue life was improved when the crack plane crossed both materials and  $Z(BM)$ , instead of a single homogeneous cross section. The observation is not derived from direct fatigue crack propagation rates, thus further work is necessary to address this anisotropy derived from the geometry of the dissimilar fusion line.

#### 4.2. Microstructural aspects of FCG through the interface

##### 4.2.1. Metastable austenite

A fundamental change in the crack driving force is apparent across the interface layer. As observed on constant  $\Delta K$  experiments, the change in propagation rates amounts up to  $-6.10E-05$  mm/cycle as the crack front crosses the fusion line between the AS steel layers into the interface. Across the AS steel material volume, the faceted nature of the crack front is clearly shown on macroscopic fractography, as shown on Fig. 3-3 and Fig. 3-4. These facets are a product of the crack front interaction with millimetre-sized grains. It has been observed that twinning and slipping control as deformation mechanism across this material volume under quasi-static fracture [37]. Fracture across austenite grains has been confirmed to occur along low index slip planes, grain and twin boundaries [55]. Thus, crystal orientations of millimetre-size crystals dictate the fracture plane through which the crack propagates, demonstrably yielding a fracture surface showing millimetre-size facets. Alternatively, the faceted fracture is lost as the crack crosses into the interface layer. The fracture morphology shown on Fig. 3-4 (e) and (f) is entirely populated by mixed quasi-cleavage and tear features, belonging to the martensite formed ahead of the crack tip. The presence of martensite is confirmed through the EBSD mapping shown on Fig. 3-6.

Available literature can give an indication on the underlying differences in fracture mode between the two material volumes. With the use of sub-millimetre CT specimens, Matsushita *et al.* [56] characterized two fundamentally different fatigue crack propagation processes distinguished by the (meta-)stability of austenite grains. For stable austenite, damage accumulation is developed as shear bands form along low-index slip systems. When enough damage is sufficiently accumulated, a shear crack propagates in a short burst along a close-packed plane, only to be slowed down while further damage is accumulated. This observation is congruent with earlier work published by Hanz and Neumann [57] and more recently by Yang *et al.* [58].

Opposingly, Matsushita *et al.* [56] also studied the fatigue crack propagation process across metastable austenite. Through their work they show how the formation and intersection of shear bands leads to the formation of  $\alpha'$ -martensite. Further deformation leads to growth of the martensite phase fraction, with most martensite laths oriented along similar crystallographic orientations. This martensite nucleation and propagation process consequently decreases the crack propagation rate. This effect is apparently only effective under stage I cracking, where  $\Delta K$  is small. Wang *et al.* [59] explain that during stage II cracking, secondary cracks are formed along martensite packet boundaries ahead of the crack tip. These secondary cracks promote crack coalescence and rapid crack propagation. Ultimately, numerous studies show that crack propagation across metastable austenite is slower compared to stable austenite under comparable loading and environmental conditions [60,61]. This observation agrees with the results obtained from constant  $\Delta K$  testing, presented in section 3.2.

##### 4.2.2. Martensite variant selection

The deformation induced martensite is different from the allotropic martensite in crystallographic terms. Based on the observations by Wang *et al.* [59] metastable austenite will transform into martensite readily decelerating the crack propagation process. The susceptibility of the austenite crystal to transform, and the selection of the child martensite phase variant will depend on the crystal and load orientations [62].

Across a material with large austenite grain sizes and strong texture such as the interface layer, under the influence of a single dominant mode of loading, strong variant selection is expected. Opposingly, the martensite derived from allotropic transformations is obtained by the thermo-mechanical strain derived from solidification and cooling. The strain conditions under which allotropic martensite is formed promote more and more diverse child variants, leading to a more ambiguous variant selection, if at all.

Distinguishing allotropic from strain induced martensite can help clarify differences in crack propagation processes. From the martensitic regions shown on Fig. 3-6, a distinction is made between based on the surroundings of the maps. Regions shown on Fig. 3-6 (a) through (c) show deformation induced martensite, while Fig. 3-6 (d) through (f) show regions populated by allotropic martensite. Fig. 3-6 (c) and (e) share the same region of interest, but a distinction is made since this region seemingly contains both allotropic and deformation-induced martensite, as obtained from a single parent austenite grain. Mapping of the identified variants assuming a K-S OR to their parent austenite grain is shown on Fig. 4-1. Alongside the variant maps, pole figures indicate the crystal directions of the twenty-four theoretically possible KS variants about the predicted orientation of the parent austenite grain. Lastly, the histogram shows the relative frequency of the variants identified. Colour coding is consistent on the maps, pole figures and histograms.

The maps shown on Fig. 3-6 indicate a clear distinction in variant selection between allotropic and deformation induced martensite. On one hand, relative frequencies of deformation-induced martensite are consistently higher for the individual variants present. On the other hand, regions of allotropic martensite show lower relative frequencies for single variants, but a more homogeneous distribution across all variants. Each region reflects in turn a selection of specific grain boundary orientation relationship between the different martensite laths. This observation is supported by the histogram presented in Fig. 4-2 (a). The figure shows the relative frequencies of all sixteen possible axis-angle relationships between martensite laths belonging to a single parent-austenite grain [63]. In accordance with the data shown on variant selection, grain boundaries show a tendency to select specific orientation relationships across the deformation induced martensite, whereas a better distribution across all possible relationships is observed across allotropic martensite. Fig. 4-2 (b) and (c) show in turn that no significant difference in terms of grain size or grain misorientation angle can be derived from the data presented. Arguably, the selection of martensite variants leads to a smaller amount of high angle packet boundaries that may restrict crack propagation. To confirm this, the fracture planes of martensite laths observed across the interface layer are studied in detail in the following subsection.

##### 4.2.3. Fracture across martensite

The microstructural mechanisms controlling fracture across martensite are now addressed. It has been discussed that the process zone ahead of the crack front induces martensite transformation across metastable austenite. Alternatively, the crack front may reach a material volume populated by allotropic martensite. In either case, crack extension will be dictated by the mechanisms governing fracture of across that phase constituent. A close inspection of the relationship between the crack path and the crystal orientation can give some indication of the mechanisms ultimately leading to fracture.

The fracture planes through which the crack propagates are analysed at select locations. Fig. 4-3 (a) and Fig. 4-3 (f) show the location on the fracture surface where ion-milled lamellae were extracted for this purpose. Transmission Kikuchi Diffraction (TKD) is used to analyse the crystal orientations of the grains subjacent to the fracture surface, as shown on Fig. 4-3 (e) and Fig. 4-3 (j). Vectors normal to the fracture trace are shown at select locations on Fig. 4-3 (b) through Fig. 4-3 (d) for the region exemplifying allotropic martensite, and Fig. 4-3 (g) through Fig. 4-3 (i) for the region exemplifying deformation-induced martensite.

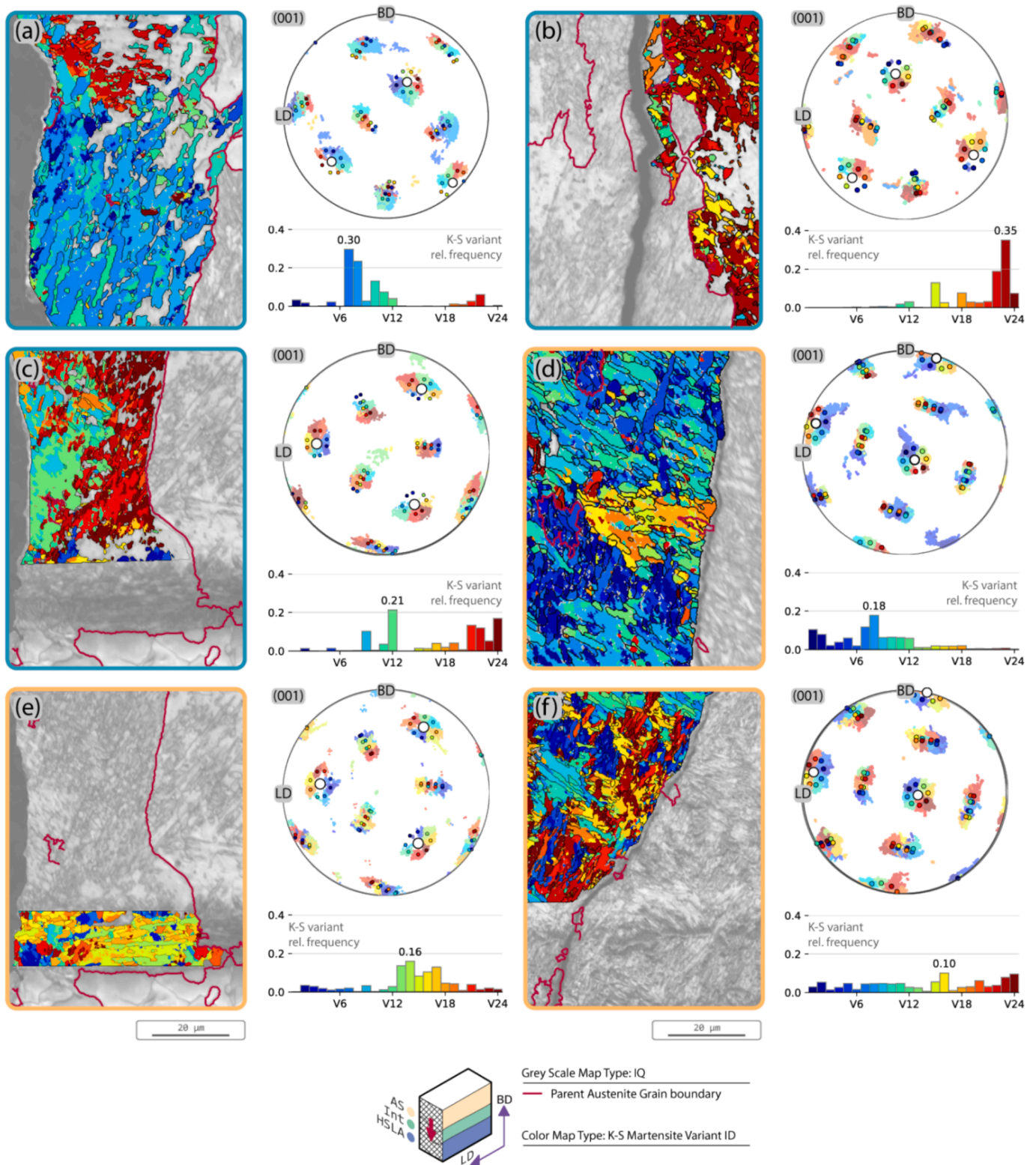


**Fig. 4-1.** Spatial distribution, (001) pole figures and relative frequency histograms of every individual K-S child variant as measured in single PAG's at the flanks of constant  $\Delta K$  fatigue cracks. All regions of interest match those shown on Fig. 3-6. Examples of deformation-induced martensite are shown in (a-c); examples of allotropic martensite are shown on (d-f). Variant maps (a-f) were obtained with a step size of 0.4  $\mu\text{m}$ .

The crystal indices parallel to the normal vectors are shown on each corresponding IPF. All points that agree with the proposed  $\langle \text{crystal index} \rangle \parallel [\text{fracture trace normal}]$  relationship within a tolerance of  $5^\circ$  are colour-plotted. Although the tolerance angle is large, it allows some room to account for the possible error induced by the lack of

perpendicularity between the section plane and the fracture surface. Indexed points outside the tolerance range are not colour-plotted.

Distinct preferences on fracture planes can be associated to the crystal structure of the adjacent martensite. The region of interest shown in Fig. 4-3 (b-d) involves two martensitic packets on the fracture plane.

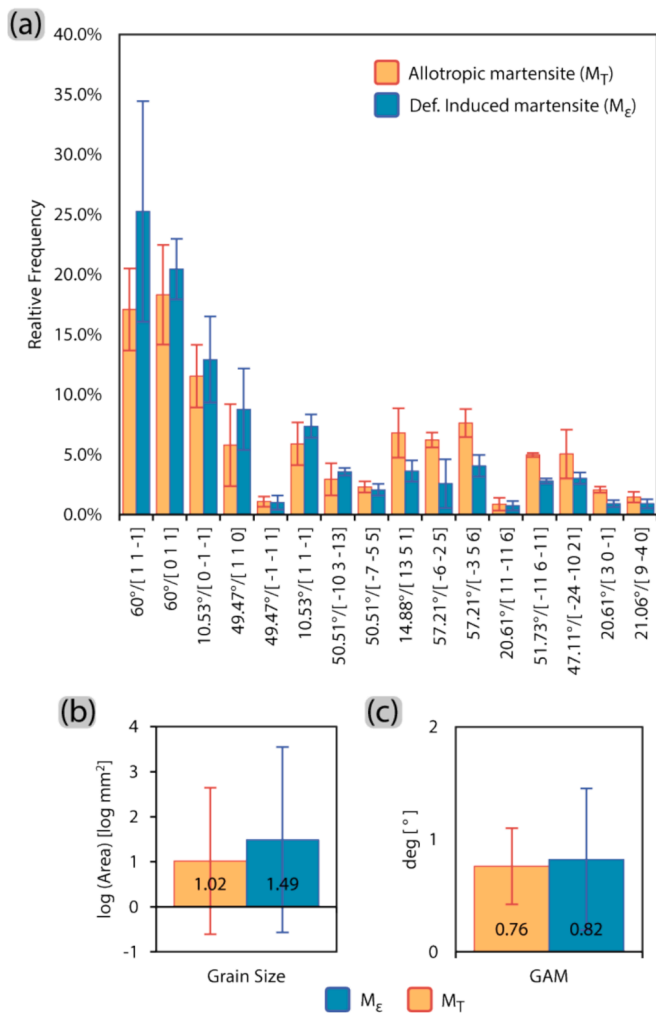


**Fig. 4-2.** (a) Relative frequency of measured axis-angle relationships possible between martensite variants, alongside grain size (b) and grain average misorientation (GAM) (c) values. Data is shown as polled from maps (a-c) for deformation-induced martensite and (d-f) for allotropic martensite.

A packet is defined as a hierarchical structure containing several blocks of martensite with the same habit plane [64]. Packet id 1 sustains a  $(111)_\gamma \parallel (011)_{\alpha'}$  relationship to its parent austenite grain. Alternatively, packet id 3 sustains a  $(\bar{1}11)_\gamma \parallel (011)_{\alpha'}$  relationship. Across packet id 1, the fracture plane agrees largely with the crystal plane family  $\{334\}$ . The adjacent martensite grains in Fig. 4-3 (b-d) belong to a packet id 3. At this location, the fracture path becomes tortuous, with fracture planes closely approximating the densely packed plane families  $\{321\}$  and  $\{112\}$ . The differences between the two packets in fracture surface development is not attributed simply to the different packets, but the habit plane that defines them [65,66]. The definition of the habit plane is a non-trivial task, but the trace of the habit plane suggests a  $\sim 40^\circ$  deviation to the notch plane. Under this condition, closed pack planes appear to be selected as fracture planes. The emergence of different martensite packets is thus beneficial, as high angle packet boundaries have been confirmed to cause crack arrest [64]. Tabulated values between the proposed fracture planes and the most proximal densely packed plane are shown on Table 4-2.

The region of interest shown in Fig. 4-3 (g-i) shows contrasting traits, that can similarly be attributed to the relationship between the martensite and apparent habit plane. The martensite packet in this region appears larger to those of allotropic martensite, and the misorientation between the fracture plane and the habit plane trace of the

martensite packages appears to be smaller ( $\sim 5.7^\circ$ ). As fracture develops across this single martensite packet, the crack propagates along high-index planes, which do not necessarily resemble any closed-packed planes. On the contrary, the crack appears to follow the block boundaries. These results agree with the observations made by Ueki et al. [61], where it is pointed out that this relationship between load and microstructure is in fact more detrimental than the one observed across allotropic martensite.

Results of this work are further supported by previous observations made on the fracture of martensite. Lindborg et al. [67] made early observations that tempered martensite fractured in well-defined planes, most frequently observed across  $\{100\}$ ,  $\{321\}$ ,  $\{211\}$  and  $\{110\}$ . This in turn depends on the carbon content and tempering conditions of the martensite laths. These cleavage fracture planes have been experimentally confirmed along the  $\{110\}$  and  $\{100\}$  planes across lath and block boundaries by Cho et al. [68] in the context of hydrogen-embrittled martensite. Moreover, the latter authors point out that the slip plane  $\{112\}$  tends to allocate deformation through dislocation accumulation. Although certain mechanisms in lath martensite have been shown to accommodate plastic deformation [69,70], TKD results confirm that transgranular fracture across close-packed planes remains the dominant mechanism controlling fracture across the allotropic martensite. The lack of capacity to accommodate and dissipate large strain results ultimately in crack acceleration, as observed in the FCGR measured through this work. Although small, the capacity to accommodate strain in lath martensite will be dependent on the relationship between the habit plane and the load direction [71]. This observation agrees with the work of Ueki et al. [60], where the authors point out that the angle between the martensite habit plane and the notch plane will dictate the fatigue crack propagation rates across this microstructural constituent. This suggests that in the context of this work, the large packets of martensite and the few variants formed ahead of the crack front across regions of metastable austenite provide small resistance to crack growth.

A multi-step sequential process is hence taking place across the interface layer. As the crack's process zone approaches metastable austenite, strain energy is spent producing deformation-induced martensite. This process leads in turn to crack deceleration. A large phase fraction of fresh metastable austenite is thus favourable to reduce FCGR rates. This effect is observed in the results presented in section 3.2, where undeformed samples show clear deceleration as the crack tip crosses into the interface layer. However, once the metastable austenite is completely transformed in the process zone ahead of the crack tip, the product martensite becomes detrimental. Because of the variant selection occurring in this process zone, this deformation-induced martensite may provide less resistance than the allotropic martensite that may be found in the crack vicinity. This observation may suggest e.g. that very high cyclic overloads in the presence of a crack could ultimately have an unproportionally detrimental effect in crack propagation rates across the interface layer.

## 5. Conclusions

Understanding the fatigue crack propagation behaviour is essential for the reliable application of HSLA-AS steel bi-material components produced by WAAM. This study provides empirical evidence on their fatigue performance. To establish a baseline, mono-material specimens of ER70S-6 (HSLA steel) and ER316L (AS steel) were benchmarked. Subsequently, fatigue crack propagation was studied across the interface layer to assess its behaviour in a bi-metal context. Techniques such as microscopy, fractography, and electron backscatter diffraction were employed to explore the relationship between microstructure and fatigue performance. Special focus is given to the martensite formed at the interface and its role, both as the product of a crack-decelerating process through TRIP effect, and as a crack accelerator in the form of allotropic martensite. Based on the results obtained, the following conclusions are drawn:

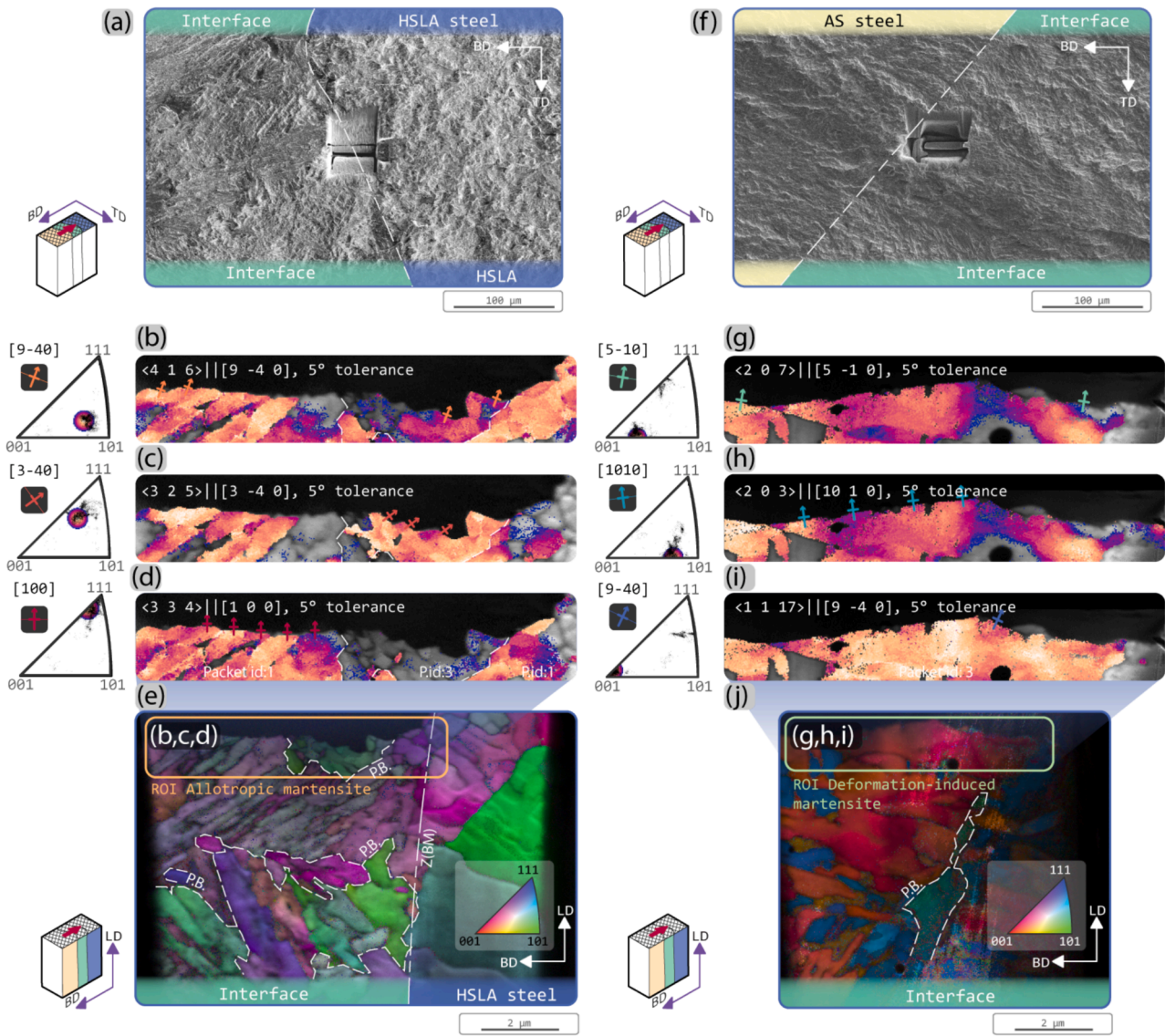


**Fig. 4-3.** TKD of FIB-milled lamella obtained from the fracture surface at the fusion line between the interface layer and the HSLA steel substrate. (a) and (f) show the locations on the fracture surface from which the lamellae were lifted (b) through (d) and (g) through (i) show the colour-mapped correspondence between proposed crystal plane and the fracture surface trace normal. Maps are shown within a 5° tolerance angle. Inverse pole figure shows colour-coding and distribution of points considered about the proposed fracture planes. (e) and (j) show the IPF mapping of the same regions as (b-d) and (g-h) and their surroundings. P.B indicates a packet boundary.

- Paris parameters and  $K_{th}$  values are provided for the interface material volume, as obtained from single edge notched bending specimens. HSLA and AS steel mono-material specimens are used to provide benchmark values. The interface is shown to have comparable Paris parameters to the mono-material counterparts, but a lower  $\Delta K_{th}$  value.
- Under constant  $\Delta K$ , the effect of the interface on the overall fatigue crack propagation performance of the bi-material specimens is made more apparent. The interface displays both a crack retardation effect at the top of the layer, and a crack accelerating effect in the vicinity of the dissimilar fusion line.
- The crack retardation effect at the interface originates from the deformation-induced martensitic transformation of metastable austenite. This process is also shown to drive variant selection on the product martensite.
- The crack acceleration process is confirmed to originate from transgranular fracture across allotropic martensite found in the vicinity of the dissimilar fusion line. It is argued that the lack of

metastable austenite restricts the work hardening capacity of the material.

- An anisotropic effect derived from the geometry of the interface layer is observed. The crack propagation process on the plane normal to the bead deposition direction (longitudinal specimen orientation, plane BD-TD) shows milder changes in FCGR.
- R ratios are shown to have an effect both on the interface layer and the HSLA steel. The driving mechanism leading to this difference is ambiguous, but a normalizing  $K^*$  parameter is used to encompass both sensitivity to  $K_{MAX}$  and  $\Delta K$ .

The results of this study contribute to the empirical evidence on the performance of functional graded bi-metal parts obtained through WAAM. By examining the transformation of the diluted interface layer into martensite and its subsequent impact on FCGR, the research elucidates the complex interplay of microstructural changes leading to crack propagation. The findings highlight the conditions under which the interface exhibits both enhanced and detrimental fatigue properties,

**Table 4.2**

Observed crystal fracture planes, their most proximal densely packed plane, and their deviation from the notch plane for ROIs shown on Fig. 4-3 (e) and Fig. 4-3 (j). Angle between the crystal plane parallel to the fracture plane and the closest densely packed plane is shown between parentheses.

ROI exemplifying allotropic martensite			ROI exemplifying deformation-induced martensite		
Crystal plane parallel to fracture plane	Closest densely packed plane	Deviation from notch plane	Crystal plane parallel to fracture plane	Closest densely packed plane	Deviation from notch plane
{416}	{213} (err. 7.61°)	-24.0°	{207}	{001} (err. 15.95°)	-11.3°
{325}	{213} (err. 4.31°)	-53.1°	{203}	{101} (err. 11.31°)	5.7°
{334}	{111} (err. 8.05°)	0°	{117}	{001} (err. 11.42°)	-24.0°

providing crucial insights for improving the design and reliability of WAAM structures with dissimilar metal interfaces.

**CRedit authorship contribution statement**

J.L. Galán Argumedo: Writing – review & editing, Writing –

**Appendix 1. Stress concentration factor**

Finite Element Analysis was used to numerically capture the effect of a sharp change in elastic modulus along the crack path in a single edge notched bending (SENB) sample. By varying the positions of the modelled crack length  $a$ , and the bi-material interface layer  $Z(BM)$ , a solution space for the elastic component of the  $J$  integral  $J_{el}$  was sought. Exploiting the symmetry around the crack plane, a model was defined in ABAQUS consisting of half an SENB sample.

The material properties chosen are isotropic and linear elastic. The diluted interface layer and the AS steel displayed an elastic modulus of 160 GPa, whereas the HSLA steel shows an elastic modulus closer to 210 GPa. These results are derived from the monotonic tests presented on [29]. The FEM models were thus fully described by two regions with different elastic moduli. Models were built for values of  $a/W$  and  $Z(BM)/W$  ranging between 0.175 and 0.850, at increments of 0.0125 in both cases. Specimen geometry and loading conditions were modelled in agreement with the experimental set up presented in section 2.2. The mesh topology, boundary conditions and elastic property assignment are shown in Fig. A1.1.

Adequate meshing and section definitions are necessary to obtain reliable  $J$  values. Quadrilateral eight-node plane strain elements with full integration were used. Symmetry boundary conditions are set along the ligament up to the crack front to reduce the number of elements. The elements around the crack tip consist of collapsed quadrilateral elements with single nodes around the tip vertex. Strain singularity around the crack tip is controlled as a function of  $1/\sqrt{r}$  by moving the mid-side nodes to the 1/4 points. The  $J$ -integral calculation relies on a series of concentric paths around the crack tip. For every geometry modelled, the  $J$ -integral is evaluated at the 10th concentric path, described by a radius approximately equal to  $0.002 \cdot W$ .

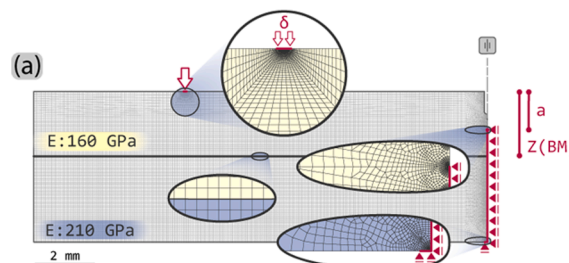


**Fig. A1.1.** Finite element model showing boundary conditions, material assignments and mesh topology, as well as the definition of the variables and .

Having obtained the elastic properties of the bi-material part through quasi-static tensile testing, it is possible to determine dimensionless relationships between the elastic properties of mono-material and the bi-material conditions. These relationships bridge the gap between the standardized solutions for fracture toughness testing of isotropic specimens and the special elastic conditions of a bi-material specimen.

The required relationship for the description of  $J_{el}$  bridges the dependency on elastic properties. Fig. A1.2 (a) and Fig. A1.2 (b) show the ratio between the results obtained from FEM analysis of a bi-material sample and the analytical expressions for  $J$ -integral available in the literature. Fig. A1.2 (a) gives the ratio between the  $J_{el}$  and  $G$  values as a function of crack tip and bi-material interface positions. The values are normalized by the

original draft, Visualization, Methodology, Investigation, Formal analysis, Data curation, Conceptualization. **A. Suresh:** Methodology, Formal analysis, Data curation. **Z. Ding:** Investigation, Formal analysis, Data curation. **V. Bertolo:** Investigation, Formal analysis, Data curation. **T.E. Reinton:** Validation, Methodology, Conceptualization. **A.C. Riemsdag:** Validation, Methodology, Conceptualization. **M.J.M. Hermans:** Writing – review & editing, Supervision, Resources, Project administration, Funding acquisition, Conceptualization. **V.A. Popovich:** Writing – review & editing, Writing – original draft, Supervision, Resources, Project administration, Funding acquisition, Conceptualization.

**Declaration of competing interest**

The authors declare the following financial interests/personal relationships which may be considered as potential competing interests: [Marcel Hermans reports financial support was provided by European Commission].

**Acknowledgements**

This project has been financed by the program of research and innovation Horizon2020 of the European Union under the grant agreement No. 862017. This research is also supported by the Materials innovation institute M2i (www.m2i.nl).

analytical solution of  $G$  describing an isotropic sample with an elastic modulus of 160 GPa. Fig. A1.2 (b) shows the same relationship for a sample with an elastic modulus of 210 GPa. These normalized relationships define  $\Gamma_J^{160}$  and  $\Gamma_J^{210}$  and are stated as follows:

$$\Gamma_J^E = \frac{J_{el,BM}}{G_{MM}^E} \quad (A1)$$

where  $J_{el,BM}$  is the numerical solution of the elastic component of J-integral for a bi-material sample and  $G_{MM}^E$  is the analytical description of elastic energy per unit area of crack extension for a mono material sample with elastic modulus  $E$ . Since  $G_{MM}^E$  is a function of the elastic modulus, a superscript 210 or 160 is used to denote the value of  $E$  used. The domain of Fig. A1.2 (a) is constrained to values were  $a/W < Z(BM)/W$ . Similarly, the Fig. A1.2 (b) is constrained to a domain of  $a/W > Z(BM)/W$ . These two conditions are set considering the geometry and loading direction of the bi-material specimens tested in this work. The following relationship is established for bi-material specimens as a basis for the definition of a bi-material stress intensity factor  $K_{BM}$ :

$$K_{BM} = \sqrt{\Gamma_J^E} \cdot K. \quad (A2)$$

where  $K$  is the stress intensity factor and  $\nu$  the Poisson's ratio. The subscript (i) is used to indicate a load-reload cycle in the single-specimen fracture toughness test procedure.

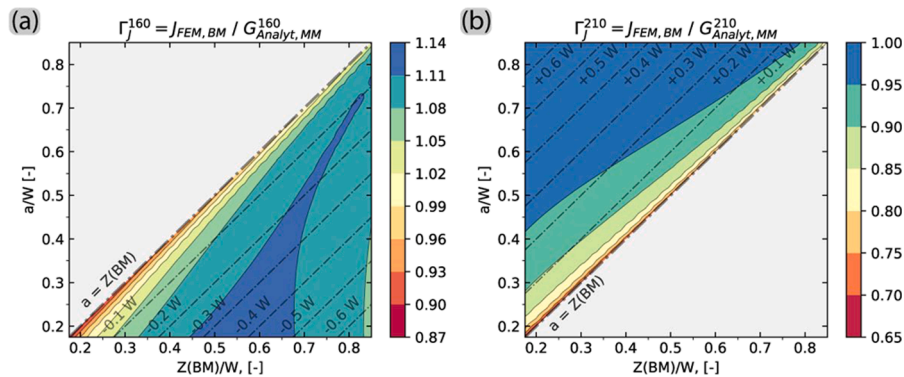


Fig. A1.2. (a) J-integral values obtained from bi-material SENB FEM model normalized by  $G$  values of a mono-material specimen with  $E = 160$  GPa as a function of crack position  $a/W$ , and position of bi-material interface  $Z(BM)$  (b) J-integral values normalized by  $G$  with  $E = 210$  GPa. Iso-distant curves of the crack front position with respect to the bi-material interface are provided each 0.1  $W$ .

## Data availability

Data will be made available on request.

## References

- [1] Ma E, Zhu T. Towards strength – ductility synergy through the design of heterogeneous nanostructures in metals. *Mater Today* 2017;20(6):323–31. <https://doi.org/10.1016/j.mattod.2017.02.003>.
- [2] Wilson JM, Shin YC. Microstructure and wear properties of laser-deposited functionally graded Inconel 690 reinforced with TiC. *Surf Coat Technol* 2012;207: 517–22. <https://doi.org/10.1016/j.surfcoat.2012.07.058>.
- [3] Popovich VA, Borisov EV, Heurtebise V, Riemslog T, Popovich AA, Sufiiarov VS. Creep and thermomechanical fatigue of functionally graded inconel 718 produced by additive manufacturing. In: *TMS 2018 147th Annual Meeting & Exhibition Supplemental Proceedings*; 2018. p. 85–97. [https://doi.org/10.1007/978-3-319-72526-0\\_9](https://doi.org/10.1007/978-3-319-72526-0_9).
- [4] Ghorbanpour S, et al. Effect of microstructure induced anisotropy on fatigue behaviour of functionally graded Inconel 718 fabricated by additive manufacturing. *Mater Charact* 2021;179:111350. <https://doi.org/10.1016/j.matchar.2021.111350>.
- [5] Carroll BE, et al. Functionally graded material of 304L stainless steel and inconel 625 fabricated by directed energy deposition: characterization and thermodynamic modeling. *Acta Mater* 2016;108:46–54. <https://doi.org/10.1016/j.actamat.2016.02.019>.
- [6] Zhang C, et al. Additive manufacturing of functionally graded materials: a review. *Mater Sci Eng A* 2019;764:138209. <https://doi.org/10.1016/j.msea.2019.138209>.
- [7] Williams SW, Martina F, Addison AC, Ding J, Pardal G, Colegrove P. Wire + Arc additive manufacturing. *Materials Science and Technology (United Kingdom)* 2016;32(7):641–7. <https://doi.org/10.1179/1743284715Y.0000000073>.
- [8] Yan L, Chen Y, Liou F. Additive manufacturing of functionally graded metallic materials using laser metal deposition. *Addit Manuf* 2020;31:100901. <https://doi.org/10.1016/j.addma.2019.100901>.
- [9] Dirisu P, Ganguly S, Mehmanparast A, Martina F, Williams S. Analysis of fracture toughness properties of wire + arc additive manufactured high strength low alloy structural steel components. *Mater Sci Eng A* 2019;765:138285. <https://doi.org/10.1016/j.msea.2019.138285>.
- [10] Rodrigues TA, Duarte V, Avila JA, Santos TG, Miranda RM, Oliveira JP. Wire and arc additive manufacturing of HSLA steel: Effect of thermal cycles on microstructure and mechanical properties. *Addit Manuf* 2019;27:440–50. <https://doi.org/10.1016/j.addma.2019.03.029>.
- [11] Rodrigues TA, et al. Steel-copper functionally graded material produced by twin-wire and arc additive manufacturing (T-WAAM). *Mater Des* 2022;213:110270. <https://doi.org/10.1016/j.matdes.2021.110270>.
- [12] Gittos M, Gooch T. The interface below stainless steel and nickel-alloy claddings. *Weld J* 1992;461–72.
- [13] Wang J, et al. Characterization of wire arc additively manufactured titanium aluminide functionally graded material: Microstructure, mechanical properties and oxidation behaviour. *Mater Sci Eng A* 2018;734:110–9. <https://doi.org/10.1016/j.msea.2018.07.097>.
- [14] Gu J, Bai J, Ding J, Williams S, Wang L, Liu K. Design and cracking susceptibility of additively manufactured Al-Cu-Mg alloys with tandem wires and pulsed arc. *Journal of Materials Processing Tech* 2018;262:210–20. <https://doi.org/10.1016/j.jmatprotec.2018.06.030>.
- [15] Dharmendra C, Shakerin S, Ram GDJ, Mohammadi M. Wire-arc additive manufacturing of nickel aluminum bronze/stainless steel hybrid parts – Interfacial characterization, prospects, and problems. *Materialia (Oxf)* 2020;13:100834. <https://doi.org/10.1016/j.mtla.2020.100834>.
- [16] Mishra A, Paul AR, Mukherjee M, Kumar R, Kumar Sharma A. Evaluation of Cu-Ti dissimilar interface characteristics for wire arc additive manufacturing process. *Rapid Prototyp J* 2023;29(2):366–77. <https://doi.org/10.1108/RPJ-05-2022-0142>.
- [17] Paul AR, Mukherjee M, Sahu MK. Influence of copper interlayer on the interface characteristics of stainless steel–aluminium transitional structure in wire arc directed energy deposition. *Rapid Prototyp J* 2024;30(1):1–14. <https://doi.org/10.1108/RPJ-03-2023-0089>.
- [18] Ahsan MRU, et al. Heat-treatment effects on a bimetallic additively-manufactured structure (BAMS) of the low-carbon steel and austenitic-stainless steel. *Addit Manuf* 2020;32:101036. <https://doi.org/10.1016/j.addma.2020.101036>.
- [19] Ayan Y, Kahraman N. Fabrication and characterization of functionally graded material (FGM) structure containing two dissimilar steels (ER70S-6 and 308LSi) by wire arc additive manufacturing (WAAM). *Mater Today Commun* 2022;33:104457. <https://doi.org/10.1016/j.mtcomm.2022.104457>.

- [20] Soysal T, Kou S, Tat D, Pasang T. Macroseggregation in dissimilar-metal fusion welding. *Acta Mater* 2016;110:149–60. <https://doi.org/10.1016/j.actamat.2016.03.004>.
- [21] Ahsan MRU, Tanvir ANM, Ross T, Elsayw A, Oh MS, Kim DB. Fabrication of bimetallic additively manufactured structure (BAMS) of low carbon steel and 316L austenitic stainless steel with wire + arc additive manufacturing. *Rapid Prototyp J* 2019;26(3):519–30. <https://doi.org/10.1108/RPJ-09-2018-0235>.
- [22] Zuback JS, Palmer TA, DeRoy T. Additive manufacturing of functionally graded transition joints between ferritic and austenitic alloys. *J Alloys Compd* 2019;770:995–1003. <https://doi.org/10.1016/j.jallcom.2018.08.197>.
- [23] J. N. DuPont and C. S. Kusko. Technical note: Martensite formation in austenitic/ferritic dissimilar alloy welds. *Welding Journal (Miami, Fla)*. 86(2), 2007.
- [24] Switzner N, Yu Z. Austenitic stainless steel cladding interface microstructures evaluated for petrochemical applications. *Weld J* 2019;98(2):50S–61S. <https://doi.org/10.29391/2019.98.004>.
- [25] Ahsan MRU, et al. Heat-treatment effects on a bimetallic additively-manufactured structure (BAMS) of the low-carbon steel and austenitic-stainless steel. *Addit Manuf* 2020;32:1–25. <https://doi.org/10.1016/j.addma.2020.101036>.
- [26] Ayan Y, Kahraman N. Fabrication and fatigue properties of dissimilar steel functionally graded material structure through wire arc additive manufacturing. *J Mater Eng Perform* 2023;32(24):11285–95. <https://doi.org/10.1007/s11665-023-07914-5>.
- [27] Suárez A, Panfilo A, Aldalur E, Veiga F, Gomez P. Microstructure and mechanical properties of mild steel-stainless steel bimetallic structures built using Wire Arc Additive Manufacturing. *CIRP J Manuf Sci Technol* 2022;38:769–73. <https://doi.org/10.1016/j.cirpj.2022.06.018>.
- [28] Allain S, Chateau JP, Bouaziz O, Migot S, Guelton N. Correlations between the calculated stacking fault energy and the plasticity mechanisms in Fe-Mn-C alloys. *Mater Sci Eng A* 2004;387–389(1–2):158–62. <https://doi.org/10.1016/j.msea.2004.01.059>.
- [29] J. L. Galán Argumedo, M. Mahmoudiniya, T. E. Reinton, L. A. I. Kestens, M. J. M. Hermans, and V. A. Popovich. Functional grading of low alloy steel to 316 L by wire arc additive manufacturing – Microstructural and mechanical characterization of bi-metal interface. *J Mater Process Technol*. 325, p. 118305, Apr. 2024, doi: 10.1016/j.jmatprot.2024.118305.
- [30] “3Dprint AM 316L. 2019. *Böhler Welding by Voestalpine*.
- [31] “3Dprint AM 46. 2018. *Böhler Welding by Voestalpine*.
- [32] Jiang W, Woo W, An G-B, Park J-U. Neutron diffraction and finite element modeling to study the weld residual stress relaxation induced by cutting. *Mater Des* 2013;51:415–20. <https://doi.org/10.1016/j.matdes.2013.04.053>.
- [33] ISO, NEN-ISO 12108 (en) Metallic materials - Fatigue crack growth mehod. Switzerland, 2018.
- [34] Ohta A, Soya I, Nishijima S, Kosuge M. Statistical evaluation of fatigue crack propagation properties including threshold stress intensity factor. *Eng Fract Mech* 1986;24(6):789–802. [https://doi.org/10.1016/0013-7944\(86\)90265-1](https://doi.org/10.1016/0013-7944(86)90265-1).
- [35] Niessen F, Nyyssönen T, Gazder AA, Hielscher R. Parent grain reconstruction from partially or fully transformed microstructures in MTEX. *J Appl Crystallogr* 2022;55(1):180–94. <https://doi.org/10.1107/S1600576721011560>.
- [36] Dirisu P, Ganguly S, Mehmanparast A, Martina F, Williams S. Analysis of fracture toughness properties of wire + arc additive manufactured high strength low alloy structural steel components. *Mater Sci Eng A* 2019;765. <https://doi.org/10.1016/j.msea.2019.138285>.
- [37] Kumar D, Jhavar S, Arya A, Prashanth KG, Suwas S. Mechanisms controlling fracture toughness of additively manufactured stainless steel 316L. *Int J Fract* 2022; 235(1):61–78. <https://doi.org/10.1007/s10704-021-00574-3>.
- [38] Gordon JV, Haden CV, Nied HF, Vinci RP, Harlow DG. Fatigue crack growth anisotropy, texture and residual stress in austenitic steel made by wire and arc additive manufacturing. *Mater Sci Eng A* 2018;724(2017):431–8. <https://doi.org/10.1016/j.msea.2018.03.075>.
- [39] Costin WL, Lavigne O, Kotousov A. A study on the relationship between microstructure and mechanical properties of acicular ferrite and upper bainite. *Mater Sci Eng A* 2016;663:193–203. <https://doi.org/10.1016/j.msea.2016.03.103>.
- [40] Ermakova A, Mehmanparast A, Ganguly S, Razavi N, Berto F. Investigation of mechanical and fracture properties of wire and arc additively manufactured low carbon steel components. *Theor Appl Fract Mech* 2020;109. <https://doi.org/10.1016/j.tafmec.2020.102685>.
- [41] Wu J, Wray PJ, Garcia CI, Hua M, Deardo AJ. Image quality analysis: a new method of characterizing microstructures. *ISIJ Int* 2005;45(2):254–62. <https://doi.org/10.2355/isijinternational.45.254>.
- [42] Suresh S, Sugimura Y, Tschegg EK. The growth of a fatigue crack approaching a perpendicularly-oriented, bimaterial interface. *Scripta Metallurgica et Materiala* 1992;27(9):1189–94. [https://doi.org/10.1016/0956-716X\(92\)90597-8](https://doi.org/10.1016/0956-716X(92)90597-8).
- [43] Sugimura Y, Lim PG, Shih CF, Suresh S. Fracture normal to a bimaterial interface: Effects of plasticity on crack-tip shielding and amplification. *Acta Metall Mater* 1995;43(3):1157–69. [https://doi.org/10.1016/0956-7151\(94\)00295-S](https://doi.org/10.1016/0956-7151(94)00295-S).
- [44] Pippan R, Riemelmoser FO. Fatigue of bimaterials. Investigation of the plastic mismatch in case of cracks perpendicular to the interface. *Comput Mater Sci* 1998; 13(1–3):108–16. [https://doi.org/10.1016/S0927-0256\(98\)00051-2](https://doi.org/10.1016/S0927-0256(98)00051-2).
- [45] Jiang F, Deng ZL, Zhao K, Sun J. Fatigue crack propagation normal to a plasticity mismatched bimaterial interface. *Mater Sci Eng A* 2003;356(1–2):258–66. [https://doi.org/10.1016/S0921-5093\(03\)00142-4](https://doi.org/10.1016/S0921-5093(03)00142-4).
- [46] Elber W. The significance of fatigue crack closure. *ASTM Spec Tech Publ STP* 1971; 486:230–42. <https://doi.org/10.1520/STP26680S>.
- [47] Martello DF, Mateo A, Chapetti MD. Crack closure and fatigue crack growth near threshold of a metastable austenitic stainless steel. *Int J Fatigue* 2015;77:64–77. <https://doi.org/10.1016/j.ijfatigue.2015.02.016>.
- [48] Donald JK. Introducing the compliance ratio concept for determining effective stress intensity. *Int J Fatigue* 1997;19(Suppl.1):191–5. [https://doi.org/10.1016/S0142-1123\(97\)00024-8](https://doi.org/10.1016/S0142-1123(97)00024-8).
- [49] Sadananda K, Nani Babu M, Vasudevan AK. A review of fatigue crack growth resistance in the short crack growth regime. *Mater Sci Eng A* 2019;754:674–701. <https://doi.org/10.1016/j.msea.2019.03.102>.
- [50] Kujawski D. A fatigue crack driving force parameter with load ratio effects. *Int J Fatigue* 2001;23(21):239–46. [https://doi.org/10.1016/S0142-1123\(01\)00158-X](https://doi.org/10.1016/S0142-1123(01)00158-X).
- [51] Li Y, Wang H, Gong D. The interrelation of the parameters in the Paris equation of fatigue crack growth. *Eng Fract Mech* 2012;96:500–9. <https://doi.org/10.1016/j.engfracmech.2012.08.016>.
- [52] Zhong Y, Xiao F, Zhang J, Shan Y, Wang W, Yang K. In situ TEM study of the effect of M/A films at grain boundaries on crack propagation in an ultra-fine acicular ferrite pipeline steel. *Acta Mater* 2006;54(2):435–43. <https://doi.org/10.1016/j.actamat.2005.09.015>.
- [53] Martello DF, Mateo AM, Chapetti MD. Fatigue crack growth of a metastable austenitic stainless steel. *Int J Fatigue* 2015;80:406–16. <https://doi.org/10.1016/j.ijfatigue.2015.06.029>.
- [54] Biswal R, et al. Interrupted fatigue testing with periodic tomography to monitor porosity defects in wire + arc additive manufactured Ti-6Al-4V. *Addit Manuf* 2019; 28:517–27. <https://doi.org/10.1016/j.addma.2019.04.026>.
- [55] Hamada AS, Karjalainen LP, Puustinen J. Fatigue behavior of high-Mn TWIP steels. *Mater Sci Eng A* 2009;517(1–2):68–77. <https://doi.org/10.1016/j.msea.2009.03.039>.
- [56] Matsushita A, Ueki S, Mine Y, Takashima K. Comparative study of microstructure-sensitive fatigue crack propagation in coarse- and fine-grained microstructures between stable and metastable austenitic stainless steels using miniature specimen. *ISIJ Int* 2021;61(5):1688–97. <https://doi.org/10.2355/isijinternational.ISIJINT-2020-659>.
- [57] Heinz A, Neumann P. Crack initiation during high cycle fatigue of an austenitic steel. *Acta Metall Mater* 1990;38(10):1933–40. [https://doi.org/10.1016/0956-7151\(90\)90305-Z](https://doi.org/10.1016/0956-7151(90)90305-Z).
- [58] Yang HK, Doquet V, Zhang ZF. Fatigue crack growth in two TWIP steels with different stacking fault energies. *Int J Fatigue* 2017;98:247–58. <https://doi.org/10.1016/j.ijfatigue.2017.01.034>.
- [59] X. Wang, C. Liu, B. Sun, and D. Ponge. The dual role of martensitic transformation in fatigue crack growth. pp. 1–7, 2022, doi: 10.1073/pnas.2110139119/-/DCSupplemental.Published.
- [60] Mei Z, Morris JW. Influence of deformation-induced martensite on fatigue crack propagation in 304-type steels. *Metallurgical transactions A, Physical metallurgy and materials science* 1990;21 A(12):3137–52. <https://doi.org/10.1007/BF02647310>.
- [61] Hornborg E. Martensitic transformation at a propagating crack. *Acta Metall* 1978; 26(1):147–52. [https://doi.org/10.1016/0001-6160\(78\)90211-0](https://doi.org/10.1016/0001-6160(78)90211-0).
- [62] De Knijf D, Nguyen-Minh T, Petrov RH, Kestens LAL, Jonas JJ. Orientation dependence of the martensite transformation in a quenched and partitioned steel subjected to uniaxial tension. *J Appl Crystallogr* 2014;47(4):1261–6. <https://doi.org/10.1107/S1600576714011959>.
- [63] Mirzaei A, et al. The role of parent austenite grain size on the variant selection and intervariant boundary network in a lath martensitic steel. *Mater Sci Eng A* 2024; 889:145793. <https://doi.org/10.1016/j.msea.2023.145793>.
- [64] Tsuboi M, Shibata A, Terada D, Tsuji N. Role of different kinds of boundaries against cleavage crack propagation in low-temperature embrittlement of low-carbon martensitic steel. *Metall Mater Trans A Phys Metall Mater Sci* 2017;48(7): 3261–8. <https://doi.org/10.1007/s11661-017-4107-9>.
- [65] Ueki S, Mine Y, Takashima K. Microstructure-sensitive fatigue crack growth in lath martensite of low carbon steel. *Mater Sci Eng A* 2020;773:138830. <https://doi.org/10.1016/j.msea.2019.138830>.
- [66] Ueki S, Matsumura T, Mine Y, Morito S, Takashima K. Microstructural fatigue crack growth in single-packet structures of ultra-low carbon steel lath martensite. *Scr Mater* 2019;173:80–5. <https://doi.org/10.1016/j.scriptamat.2019.08.004>.
- [67] Lindborg UH, Averbach BL. Crystallographic aspects of fracture in martensite. *Acta Metall* 1966;14(11):1583–93.
- [68] Cho L, et al. Characteristics and mechanisms of hydrogen-induced quasi-cleavage fracture of lath martensitic steel. *Acta Mater* 2021;206:116635. <https://doi.org/10.1016/j.actamat.2021.116635>.
- [69] Ueki S, Mine Y, Lu X, Chiu YL, Bowen P, Takashima K. Effect of geometric lath orientation on fatigue crack propagation via out-of-plane dislocation glide in martensitic steel. *Scr Mater* 2021;203:114045. <https://doi.org/10.1016/j.scriptamat.2021.114045>.
- [70] Du C, Hoefnagels JPM, Vaes R, Geers MGD. Plasticity of lath martensite by sliding of substructure boundaries. *Scr Mater* 2016;120:37–40. <https://doi.org/10.1016/j.scriptamat.2016.04.006>.
- [71] Mine Y, Hirashita K, Takashima H, Matsuda M, Takashima K. Micro-tension behaviour of lath martensite structures of carbon steel. *Mater Sci Eng A* 2013;560: 535–44. <https://doi.org/10.1016/j.msea.2012.09.099>.